Data-driven modeling of solar coronal magnetic field evolution and eruptions
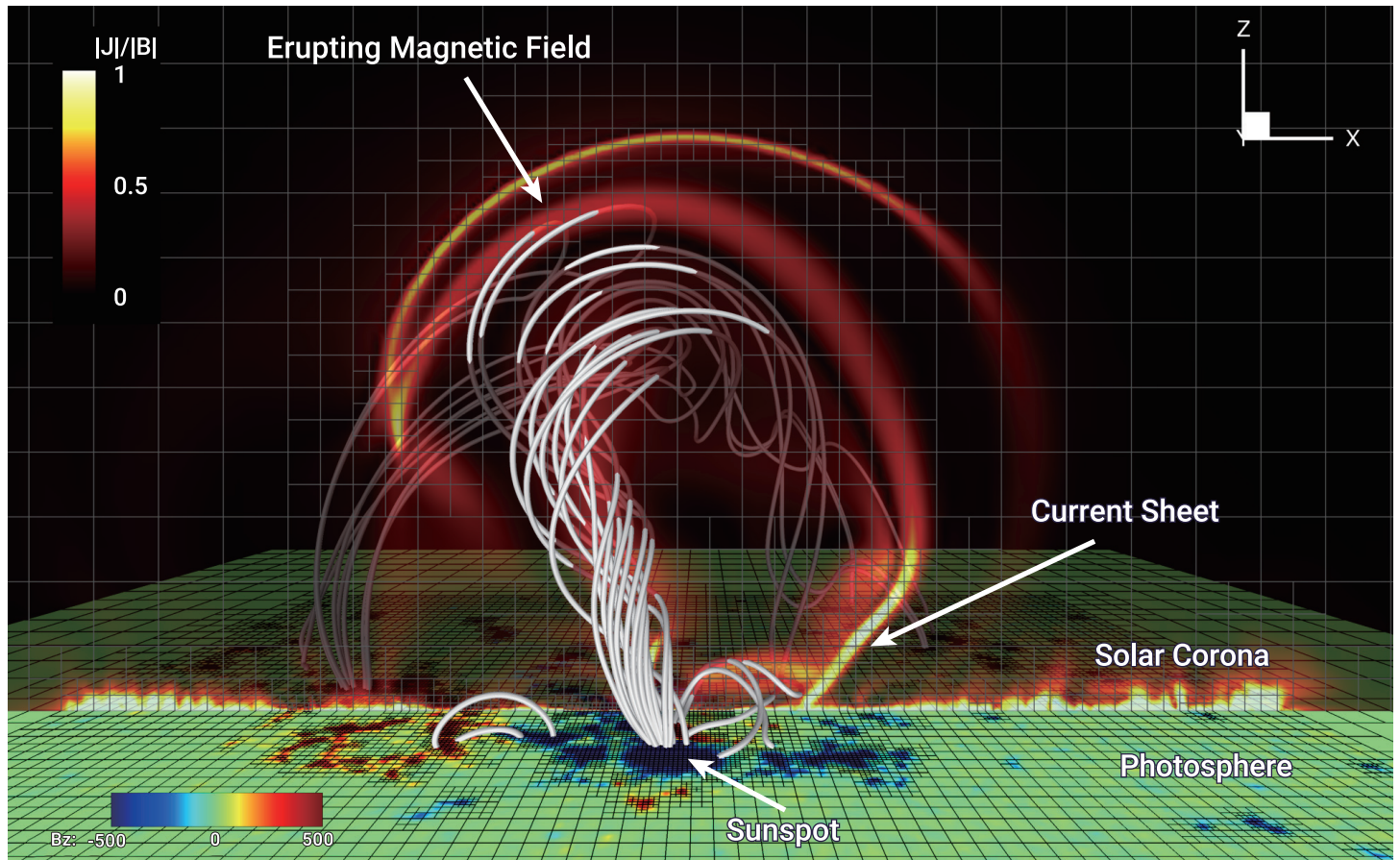
Chaowei Jiang,[1,*] Xueshang Feng,[1] Yang Guo,[2] and Qiang Hu[3]

*Correspondence: chaowei@hit.edu.cn

GRAPHICAL ABSTRACT

PUBLIC SUMMARY

- Data-driven models offer a novel avenue to study solar coronal magnetic fields

- Such numerical models are directly driven by continuously-observed magnetograms

- They are able to reproduce the magnetic structures and evolutions of solar eruptions

- They help shed new light on the physical mechanisms of complex solar eruptions

Data-driven modeling of solar coronal magnetic field evolution and eruptions

Chaowei Jiang,[1,*] Xueshang Feng,[1] Yang Guo,[2] and Qiang Hu[3]

[1]Institute of Space Science and Applied Technology, Harbin Institute of Technology, Shenzhen 518055, China
[2]School of Astronomy and Space Science, Nanjing University, Nanjing 210023, China
[3]Department of Space Science, The University of Alabama in Huntsville, Huntsville, AL 35899, USA
*Correspondence: chaowei@hit.edu.cn

Magnetic fields play a fundamental role in the structure and dynamics of the solar corona. As they are driven by their footpoint motions on the solar surface, which transport energy from the interior of the Sun into its atmosphere, the coronal magnetic fields are stressed continuously with buildup of magnetic nonpotentiality in the form of topology complexity (magnetic helicity) and local electric currents (magnetic free energy). The accumulated nonpotentiality is often released explosively by solar eruptions, manifested as solar flares and coronal mass ejections, during which magnetic energy is converted into mainly kinetic, thermal, and nonthermal energy of the plasma, which can cause adverse space weather. To reveal the physical mechanisms underlying solar eruptions, it is vital to know the three-dimensional (3D) structure and evolution of the coronal magnetic fields. Because of a lack of direct measurements, the 3D coronal magnetic fields are commonly studied using numerical modeling, whereas traditional models mostly aim for a static extrapolation of the coronal field from the observable photospheric magnetic field data. Over the last decade, dynamic models that are driven directly by observation magnetograms have been developed and applied successfully to study solar coronal magnetic field evolution as well as its eruption, which offers a novel avenue for understanding their underlying magnetic topology and mechanism. In this paper, we review the basic methodology of the data-driven coronal models, state-of-the-art developments, their typical applications, and new physics that have been derived using these models. Finally, we provide an outlook for future developments and applications of the data-driven models.

INTRODUCTION

The solar corona, the upper atmosphere of the Sun, consists of highly magnetized, hot plasma with temperatures of millions of degrees.[1] Observations using soft X-ray and extreme ultraviolet (EUV) emissions of this plasma indicate that the magnetic field in the corona has a complex and evolving structure that is continuously driven by the ceaseless motions at the solar surface, the photosphere, by which energy is transported from the interior of the Sun to the corona. During this process, the coronal magnetic field is stressed, electric current is built up, and magnetic free energy is accumulated continuously. From time to time, magnetic explosions, known as solar eruptions, are produced as a result of the rapid release of this magnetic energy into thermal and kinetic energy.[2,3] The most violent eruptions manifest as major solar flares and coronal mass ejections (CMEs). They unleash a huge amount of magnetic flux (on the order of 10^{14} Wb or 10^{22} Mx, the same order of magnetic flux contained in a typical solar active region) and plasma (with a mass of $10^{11} \sim 10^{13}$ kg, similar to the mass of a typical solar filament or prominence[4] into the heliosphere[4] and drive adverse space weather events that could severely affect human activities in modern society.

It has long been recognized that magnetic fields play a fundamental role in almost all dynamics in the solar corona, such as formation of coronal loops and prominences (or filaments), initiation of solar eruptions, as well as modulation of the global structure of solar wind.[5] However, it remains very difficult to make a direct measurement of the coronal magnetic fields from emissions of the extremely tenuous plasma in the corona by traditional spectro-polarimetric methods (using the Zeeman and Hanle effects). There are attempts made to measure coronal fields using infrared wave bands[6] and radio emissions[7–9] as well as coronal seismology[10] (or magnetoseismology[11,12]), but these can only give fragmentary and occasional data. Another way has been proposed to measure coronal fields, using magnetically induced transitions of EUV lines (e.g., Fe X and Fe XI), but the accuracy of determination of field strength would be of the order of the magnitude.[13,14] Up to the present, routine measurement of the Sun's

magnetic field that we can rely on is restricted to only a single layer of the solar atmosphere, i.e., the photosphere (the photosphere still has a finite thickness, but it is extremely small compared with the length scales in the corona).

The concept of numerically modeling the three-dimensional (3D) coronal magnetic field with the bottom boundary constrained by the observed photospheric magnetograms dates back to over half a century ago.[15] The earliest model used a lowest-order assumption that the coronal field is current free (namely, a potential field), whereas almost all modern codes for coronal magnetic field reconstruction (or extrapolation) are based on the more realistic assumption that the Lorentz force vanishes in the corona (i.e., the magnetic pressure force and magnetic tension force balance each other). This is because in most parts of the low corona (with a height of less than ∼400 Mm from the coronal base), particularly in the strongly magnetized active regions (ARs), the plasma β (the ratio of plasma thermal pressure to magnetic pressure) is low (with typical values of 10^{-4} to 10^{-2}), and all other forces can be neglected compared with the magnetic pressure gradient force (or magnetic tension force). Over the past several decades, a variety of nonlinear force-free field (NLFFF) extrapolation codes that use vector magnetograms as the key input have been developed and have greatly improved our knowledge of the 3D structure and topology of the coronal magnetic fields, which is extensively discussed in a few review papers.[16–19] The NLFFF models have major limitations, and one of them is due to the basic assumption that the coronal magnetic field always remains in a static equilibrium. Such a Lorentz force balance is strongly violated during solar eruptions, in which the magnetic field evolves rapidly with Alfvénic speed as driven by the unbalanced Lorentz force. The interaction of the magnetic field with plasma is totally omitted in the NLFFF and other similar static extrapolation models, and thus they cannot be used to study dynamics associated with the temporal evolution of the corona. Another limitation of some NLFFF models, especially of those employing an iteration approach and assuming a potential field as the initial guess, would be that it may be difficult to reach the solution when the actual coronal fields are highly deviated from the potential field (such as those including magnetic flux ropes).

The macroscopic behavior of coronal dynamic evolution is described self-consistently by magnetohydrodynamics (MHD) equations, which characterize the nonlinear interaction of the magnetic field with plasma.[20,21] In recent years, time-dependent models based on MHD (or its simplifications) and using continuously observed magnetograms as input have arisen to reproduce the dynamics of the corona. Such data-driven models are a significant step forward in coronal magnetic field modeling compared with traditional methods, providing a novel avenue to study coronal magnetic evolution, including slow, quasi-static coronal evolution as driven by photospheric motions, the rapidly evolving field in solar eruptions, and the self-consistent transition from a quasi-static stable equilibrium to fast eruption. In this paper, we review the basic methodology of data-driven coronal models, state-of-the-art developments, their typical applications, and new physics that have been derived using these models. This review is focused on low coronal evolution and mainly on the scale of ARs with emphasis on solar eruptions.

DIFFERENT MODELS

All current data-driven models can be classified mainly into three groups with increasing degrees of complexity and, thus, realism. They are the magnetofrictional model,[22–33] the zero-β MHD model,[34–39] and the full MHD model.[40–50] The full MHD model can be divided into subclasses, such as isothermal, ideal, resistive, and full thermodynamic (including radiation and thermal conduction) models according to the different types of energy equations.

The magnetofrictional model

The magnetofrictional model was originally proposed for NLFFF reconstruction.[51] It is the computationally cheapest way (and, thus, the most frequently used one) to carry out data-driven simulations by assuming that the coronal magnetic field evolves slowly as a continuous series of force-free equilibria. To derive this model, an artificial frictional force $\nu_f\,\rho\mathbf{v}$ (where ν_f is the frictional coefficient, ρ the plasma density, and $\mathbf{v}$ the velocity) is included in the MHD equation of motion,

$$\rho\frac{D\mathbf{v}}{Dt} = -\nabla p + \rho\mathbf{g} + \mathbf{j}\times\mathbf{B} - \nu_f\rho\mathbf{v},$$

where p, $\mathbf{g}$, $\mathbf{j}$, and $\mathbf{B}$ are the thermal pressure, the solar gravity, the electric current density, and the magnetic field, respectively. Then, by neglecting the thermal pressure, the gravitational force, and the inertial effect, this equation can be reduced to expression of the so-called magnetofrictional velocity:

$$\mathbf{v} = \frac{1}{\nu_f\rho}\mathbf{j}\times\mathbf{B}.$$

The magnetofrictional velocity acts to ensure that the magnetic field remains close to a force-free equilibrium as the field is perturbed via boundary motions. A pseudo-density is assumed to be $\rho = B^2$ (thus, a uniform pseudo Alfvén speed; the pseudo density is usually absorbed into the frictional coefficient), and the only equation that needs to be solved is the induction equation (Faraday's law),

$$\frac{\partial\mathbf{B}}{\partial t} = -\nabla\times\mathbf{E} = \nabla\times(\mathbf{v}\times\mathbf{B} - \eta\mathbf{j}),$$

where $\mathbf{E}$ is the electric field, and $\eta\mathbf{j}$ is the resistivity term which can be omitted for an ideal process. To fulfill the solenoidal requirement of $\mathbf{B}$, the vector potential $\mathbf{A}$ (with a Coulomb gauge; i.e., $\nabla\cdot\mathbf{A} = 0$) can be used as the primary variable (thus, $\mathbf{B} = \nabla\times\mathbf{A}$), and the induction equation is then written as[23,26,32]

$$\frac{\partial\mathbf{A}}{\partial t} = -\mathbf{E} = \mathbf{v}\times\mathbf{B} - \eta\mathbf{j}.$$

A central difference scheme with a staggered grid[52] can be used to calculate the spatial derivatives, and then a forward difference in time is used to advance the solution. The time step should be determined by the largest Alfvén speed, complying with the Courant-Friedrichs-Lewy (CFL) condition. There are different choices for the frictional coefficient, which determines the relaxation speed of the system (some use a constant value[26,32] and others use a height-dependent value[22,23,27,28]) to optimize the match between simulations and observations. The initial value of the magnetic field can be obtained from static extrapolations (e.g., a potential field or more sophisticated NLFFF if needed).

Compared with other models, the magnetofrictional model is a convenient way to follow the quasi-static coronal evolution, but it should be noted that this model, in principle, cannot be used to simulate eruptions whose dynamics are far away from a force-free state. Another serious issue of the magnetofrictional model, as recently pointed out by Yeates,[53] is that it might lead to breakdown of magnetic flux conservation even when using an ideal induction equation.

Zero-β MHD model

The zero-β MHD model is also a simplified version of the MHD model. It omits the non-Lorentz forces of gas pressure gradient and solar gravity in the equation of motion, which thus reads as

$$\rho\frac{D\mathbf{v}}{Dt} = \mathbf{j}\times\mathbf{B} + \nabla\cdot(\nu\rho\nabla\mathbf{v}),$$

where a viscosity term is often included for the purpose of fast relaxation (and numerical stabilization). In some works, a pseudo-density similar to that in the magnetofrictional model (for example, $\rho = B^2$ or $\rho = B$) is used;[37,54] thus, only this simplified momentum equation along with the induction equation need to be solves. Others[35,38,39,55,56] also solve the continuum equation

$$\frac{\partial\rho}{\partial t} + \nabla\cdot(\rho\mathbf{v}) = 0,$$

with an initial *ad hoc* setting of the density like $\rho_0 \propto B_0^{3/2}$ (where B_0 is the initial magnetic field strength), aimed at mimicking the profile of the coronal Alfvén speed,[56] or a more realistic one that employs the stratified density profile from the photosphere to the corona;[35] thus, the observed photospheric magnetic field can be handled at the bottom boundary directly. The zero-β model can be solved using existing full MHD codes; for example, the data-driven model developed by Guo et al.[35] is built on an open-sourced parallelized, adaptive mesh refinement (AMR) code for MHD, MPI-AMRVAC.[57,58]

By discarding the thermal pressure (and, thus, the energy equation), the zero-β model can be solved more efficiently than the full MHD model, and it avoids the particular numerical problem of negative pressure potentially arising in the very low-β region. But the caveat is that the zero-β assumption is reasonable only in domains where the plasma β is extremely low, whereas the real β in the corona is quite variable;[59] for example, there are also places with considerably high β in the corona because of the prevalence of magnetic null points. Relevant to this limitation is that, for studying eruptions, the zero-β assumption might fail when there is a fast reconnection in the field, in which the thermal pressure could play an important role in dynamics in the weak-field region of magnetic field dissipation.

The full MHD model

The full MHD model solves all equations, including the continuum equation, the momentum equation, the induction equation, as well as the energy equation, and thus has none of the limitations mentioned for the magnetofrictional and zero-β models, but, of course, the computational cost will be higher. The full MHD equations as used by different authors differ mainly in the last equation (i.e., the energy equation), which can take various forms, using different assumptions for particular purpose. For instance, an adiabatic process is often considered when focusing on the evolution of the magnetic field and its interaction with plasma; e.g., using a temperature equation,[44,60]

$$\frac{\partial T}{\partial t} + \nabla\cdot(T\mathbf{v}) = (2-\gamma)T\nabla\cdot\mathbf{v},$$

where T is the temperature and γ the polytropic index. By letting $\gamma = 1$, it reduces to the isothermal process.[61] More comprehensive thermodynamics could be included, such as the radiation, thermal conduction, and (parameterized) coronal heating processes,[42,47,62,63] to build data-driven radiative MHD model.[64,65] For localized simulation of AR scales, the initial conditions often consist of an isothermal[44,60] or temperature-stratified[42,47,66] atmosphere in a hydrostatic state and a potential or near force-free magnetic field. Aimed at mimicking the highly non-uniform distribution of plasma in the corona, some models[48] also use a pre-initial density proportional to local magnetic field strength and let the MHD system evolve to a new equilibrium, which is then used as the initial state of subsequent data-driven simulation. For a global simulation that includes solar wind, the initial conditions are usually obtained by relaxing the Parker's spherically symmetric solution of solar wind along with a global potential field to a steady state. Although the classical finite difference method can be used,[42,47] numerical integration of the MHD equations is more commonly implemented using the modern, Godnuov-type finite volume scheme; for example, the total variation diminishing (TVD) Lax-Friedrichs formulation[67] and the monotonic upstream scheme for conservation laws[68] based on characteristic decomposition and Riemann solver. A recently developed scheme, the space-time conservation element and solution element (CESE) method,[69–71] has also been used efficiently in data-driven MHD models with features of massive parallel computing and AMR.[41,44,45]

THE DATA-DRIVEN BOUNDARY CONDITIONS

The unique feature that distinguishes a data-driven coronal model from others is incorporation of the observables of a time sequence directly into the model. This is realized by specifying time-dependent boundary conditions at the bottom surface using the continuously observed data as provided there. Ideally, all independent variables that are required to be solved in the controlling equations of the specific models should be provided self-consistently for the bottom boundary by observations.[72] However, because of the limited observations, these boundary conditions are underspecified, and, thus, different implementations use different assumptions, which currently can be classified into mainly three types. The first choice, $\mathbf{B}$ driven, is to give the observed photospheric magnetic field data directly as the boundary values. The second one, $\mathbf{V}$ driven, is to determine the plasma flow at the photosphere and to drive the simulated magnetic field through the
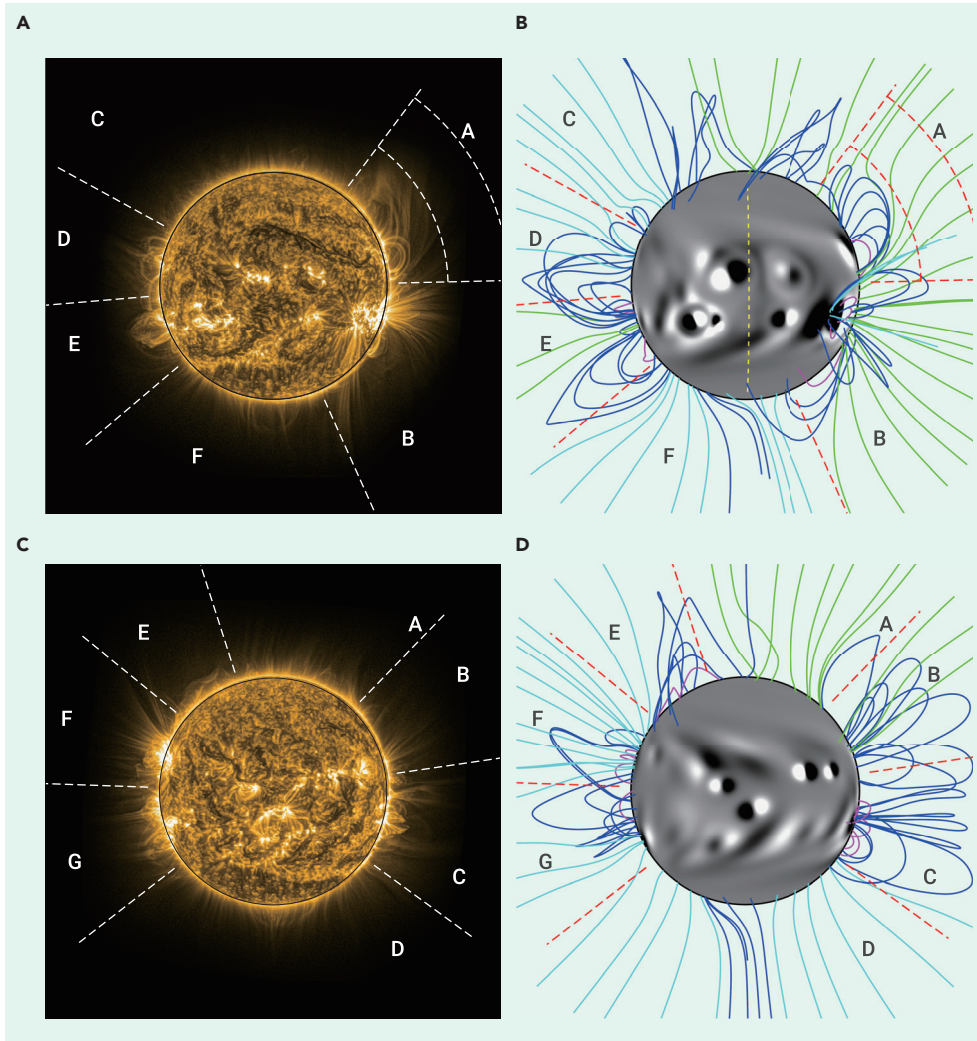
Figure 1. Comparison of EUV images of the global corona with magnetic field lines from a data-driven magnetofrictional simulation (A–D) Observations from Sun Watcher using the Active Pixel System detector and Image Processing (SWAP) instrument on board the Project for Onboard Autonomy 2 (PROBA2) spacecraft (A and C)[82] and simulation results (B and D). Shown are data for October 27, 2014 (A and B) and November 4, 2014 (C and D). In (A) and (B), the white dashed lines and letters A–F indicate zones for comparison. The dashed arcs in zone A in (A) are plotted at 0.54 R_S (i.e., solar radius) and 1.07 R_S above the photosphere. In (B) and (D), the photospheric magnetic field B_r is shown by the black and white colors saturated at ±30 Gauss, and a selection of coronal magnetic field lines are shown in magenta (closed, low lying), dark blue (closed), green (open, positive field), and light blue (open, negative field). Image reproduced from Meyer et al.[81]

MDI magnetograms, quantified the free energy accumulation as driven by the magnetic flux dispersal, and concluded that the injected free energy is sufficient to explain the radiative losses at coronal temperatures within the AR. Using data from the Helioseismic and Magnetic Imager (HMI) onboard Solar Dynamics Observatory (SDO)_and data from Sunrise balloon-borne observatory, Chitta et al.[80] applied a similar model to study the spatial and temporal variations of the energy dissipation rate and energy flux in a quiet region. They found that the energy deposited in the solar atmosphere is concentrated mostly near the photosphere (within a height of only 2 Mm) and that there is no sufficient energy flow upward to balance radiative and conductive losses in the corona. The data-driven magnetofrictional model has also been extended to the global corona to study the non-potential energy evolution of the global magnetic field[30] and to reproduce the large-scale magnetic topology with full-disk EUV images (Figure 1) for the middle corona[81] over a few Carrington rotations.

Other studies using the magnetofrictional models are devoted to formation and evolution of the eruptive structure, in particular, magnetic flux rope (MFR), which is commonly believed to be an important candidate for the pre-eruptive magnetic structures.[83–89] Cheung and DeRosa[23] performed simulations of the flux-emerging AR NOAA 11158 and found that, when continuous twisting is imposed at the bottom boundary (through an assumed form of electric field), the AR can form a series of flux rope ejections from the central polarity inversion line (PIL). Using a proxy emissivity based on the LOS integration of the field-line averaged square of current density, they were able to produce synthesis images with a visual texture similar to EUV images of coronal loops (Figure 2). Cheung et al.[22] modeled a recurrent MFR formation during the emergence of a current-carrying magnetic field that produced homologous helical jets. Gibb et al.[24] modeled how a sigmoidal MFR is built up in the decaying phase of AR NOAA 10977 through continual flux cancellation.[90] Yardley et al.[32] simulated nearly the full life of AR NOAA 11437 (5 days) from its initial emergence to decay phases, in which MFRs were also found to form and erupt. By parameterized tests of different non-inductive electric field entered at the boundary for simulation of AR NOAA 11504, Pomoell et al.[27] showed that MFRs can form and erupt only with an enhanced injection of magnetic helicity. They also found that the coronal evolution appears to be significantly different with different helicity injections despite relatively similar total energy injections because the helicity quantifies the overall degree of complexity of the field structure. Price et al.[28] used the same data-driven approach to study formation of an unstable MFR in the rapid and complex flux-emerging AR NOAA 12673, which produced the largest flare in solar cycle 24. An interesting finding is that the evolution of magnetic helicity in the simulation suggests a possible threshold for eruptions in the ratio

ideal induction equation, $\partial_t \boldsymbol{B} = \nabla \times (\boldsymbol{v} \times \boldsymbol{B})$, or other ways. The third choice, $\boldsymbol{E}$ driven, is to determine the electric field $\boldsymbol{E}$ and to drive the magnetic field as $\partial_t \boldsymbol{B} = -\nabla \times \boldsymbol{E}$. A combination of different choices also exists; for example, by specifying simultaneously the observed magnetic field and the derived velocity at the bottom boundary. A detailed description of the implementation of these boundary conditions is given in the supplemental information.
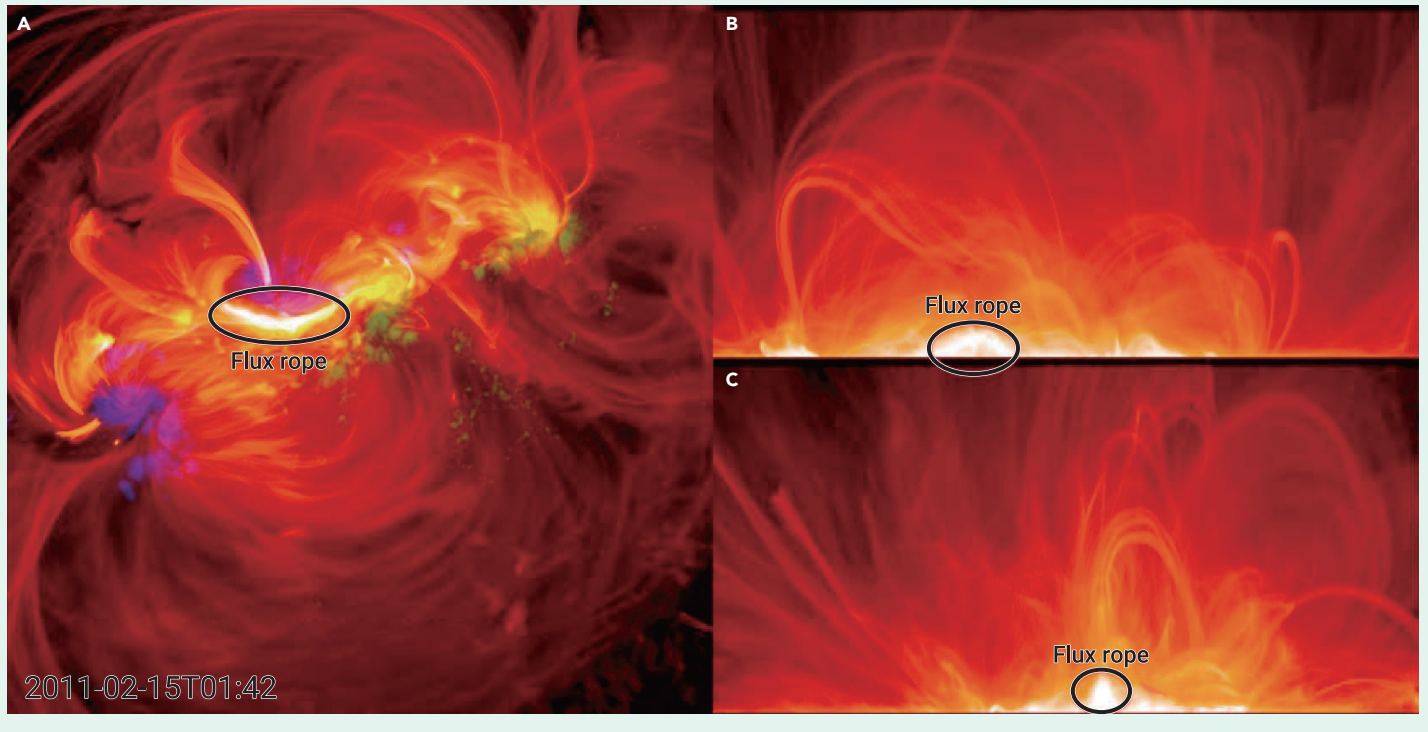
DATA-DRIVEN MODELING OF THE SLOW EVOLUTION OF CORONAL MAGNETIC FIELDS

In a period without eruptions, the coronal magnetic fields evolve in a quasi-static way, driven by the slow motions at the photosphere. Although such an evolution could be approximately followed by a time series of independent NLFFFs[73–75] or MHD equilibria,[40,49,76,77] the data-driven model produces a continual evolution that allows a "memory" of magnetic connectivity and build-up of electric currents and free magnetic energy. Wu et al.[48,78] studied the realistic evolution of ARs using a data-driven full MHD model for the first time. Their model is driven by the line-of-sight (LOS) magnetograms from the Michelson Doppler Imager (MDI) onboard Solar and Heliospheric Observatory (SOHO) and includes the effects of differential rotation and meridional flow, and concluded that, for the studied AR, the surface transverse flow plays a dominant role in magnetic energy flux through the photosphere.

Because the full MHD simulation is time consuming, the computationally faster magnetofrictional models, which utilize LOS or vector magnetograms, are used widely to follow the long-term quasi-static evolution of ARs; e.g., a few days during which ARs build up their nonpotentiality. Some of the works are focused on the magnetic energy injection from the photosphere into the upper atmosphere, which can shed light on the coronal heating problem.[79] Mackay et al.[26] modeled the decaying phase of AR NOAA 8005 using SOHO/

Figure 2. Synthetic images of coronal loops based on current density distribution from a data-driven magnetofrictional model for the evolution of AR NOAA 11158 (A–C) The same data from different viewing angles. (A) Top view. (B) Side view perpendicular to the spine of the MFR. (C) Side view along the spine. The time as shown is selected when an erupting flux rope from the model is just starting to lift off, which is near the onset time of an eruptive X2.2 flare in the AR. Image reproduced from Fisher et al.[94] with permission from AGU.

of current-carrying helicity to relative helicity.[91,92] Price et al.[29] further simulated an MFR formed in AR NOAA 12473 and found it became torus unstable[93] before the eruption. Kilpua et al.[25] analyzed the details of an MFR eruption in AR NOAA 12158 and attempted to compare its structure (but still in the source region) with *in situ* observations at 1 AU.

Although many studies using the data-driven magnetofrictional model also claimed simulation (or even reproduction) of eruptions, the magnetofrictional model cannot self-consistently model the eruptive dynamics because of the inherent limitations of the model; i.e., the assumption that the coronal field evolves quasi-statically. First, the strong frictional force in the model can quickly slow down any unstable structure that tends to erupt, especially considering that there is no inertial effect. Thus, the erupting structure moves very slowly. For example, as shown in the simulation of a torus-unstable MFR by Price et al.,[29] the MFR takes over 4 days to ascend a height of about 100 Mm, which otherwise should only take a few minutes in a realistic eruption. Second, the fast reconnection,[95] which is responsible for the impulsive release of free magnetic energy into kinetic energy, which powers the eruption, cannot happen in the magnetofrictional model. So these simulations ignored the important role of fast reconnection in driving the eruption that is proposed in many theoretical models of eruption.[96–99] Therefore, it is more appropriate to use the pre-eruptive field as simulated in the magnetofrictional model as an initial condition to a more self-consistent full MHD model for the purpose of simulating eruptions.[100]
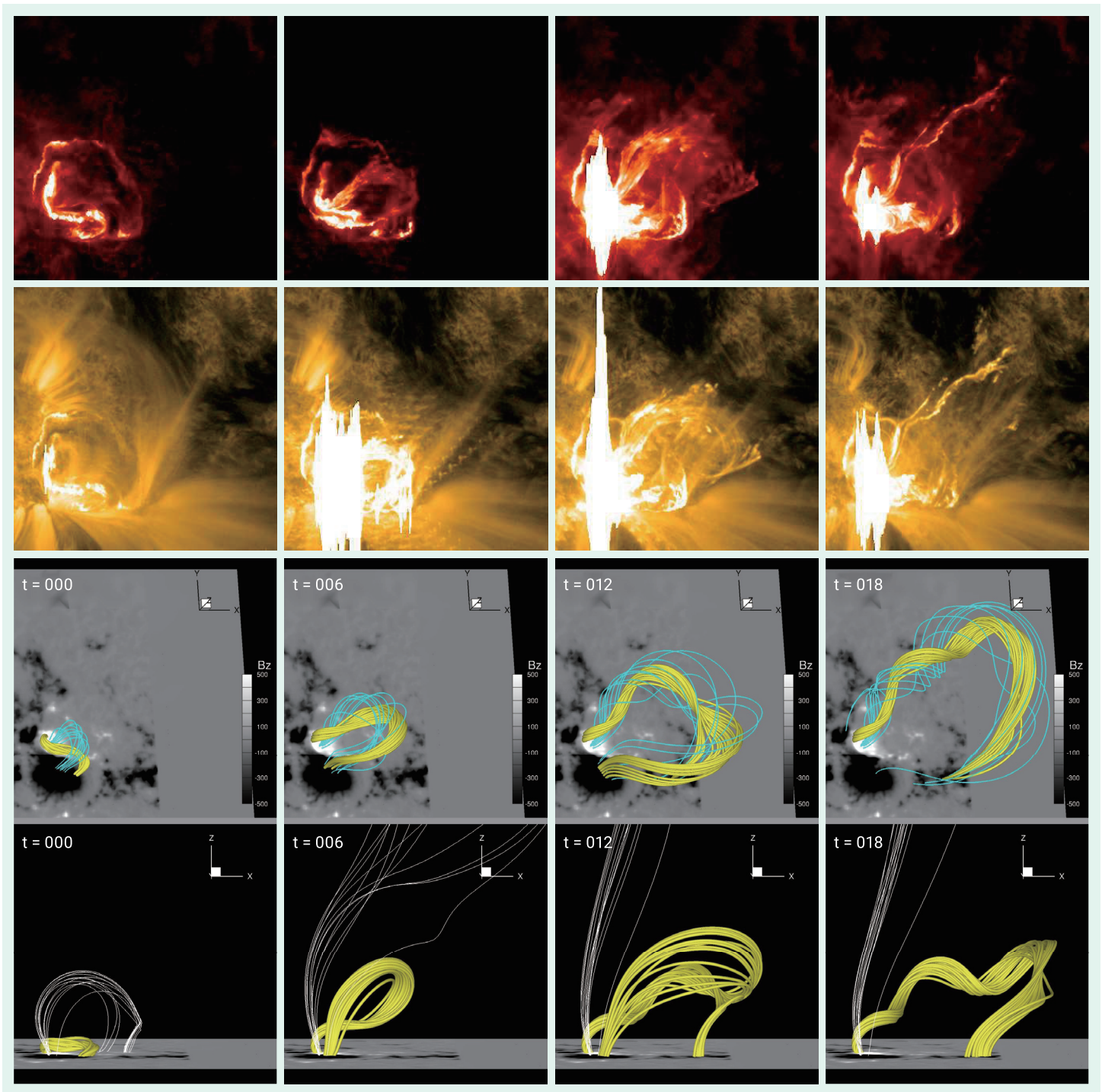
SIMULATION OF SOLAR ERUPTIONS

The MHD simulation initialized with unstable (or close to unstable) magnetic field data that are extrapolated for a time shortly prior to an eruption proves to be a very useful approach to realistically reproduce the subsequent eruptive process, which has been shown by Jiang et al.[101] when studying the eruption of a sigmoidal MFR in AR NOAA 11283. Strictly speaking, such a simulation cannot be considered a data-driven model because only a single set of magnetograms is used (thus, data constrained would be more appropriate), but we regard it as a quasi-data-driven model by considering that the initial condition is constructed using data, and it is the initial instability that drives the evolution. Because, with just a single snapshot of a magnetogram, such a type of model is only valid for a short period (e.g., a few minutes, focusing only on the eruption process), during which

the photospheric driving effect (e.g., the surface motion and flux emergence and cancellation) can be neglected.

Analysis of the pre-flare NLFFF extrapolated from the SDO/HMI vector magnetogram based on their CESE-MHD-NLFFF code,[54,102,103] Jiang et al.[101] show that AR NOAA 11283 has a spine-fan topology of magnetic null point, linking multiple polarities and an MFR, which is close to torus instability (TI),[93] is embedded in the complex topology. When entered in the MHD model (although with a fixed bottom boundary), the field erupts, driven by the TI, and is accelerated by the breakout-type reconnection[96] at the null. The initiation and subsequent evolution of the eruptive flux rope resemble remarkably in morphology the corresponding EUV features, such as the sigmoid, the filament ejection, as well as quasi-circular flare ribbons, as observed by the Atmospheric Imaging Assembly (AIA[104]) on board SDO (Figure 3). This result has two-fold significance. On one hand, it evidences the agreement of the extrapolated field with the realistic corona prior to eruption; on the other hand, it shows the reliability of the MHD model in characterizing the dynamics during eruptions. Because previous simulations of solar eruptions before Jiang et al.[101] were commonly carried out with idealized or hypothetical magnetic field configurations, the combination of NLFFF and MHD models provides a viable way to reproduce realistic eruption process with complexity that is beyond the scope of idealized or theoretical models.

A similar way of simulating realistic eruptive events has been employed by many modelers with different pre-flare coronal field reconstructions (on which the performance of such kind of simulation largely depends), different MHD codes, as well as different boundary conditions.[35–37,39,73,100,105–112] For example, Kliem et al.[110] studied the first eruptive event witnessed by SDO using an unstable NLFFF constructed with the flux rope insertion technique[113,114] to initialize a zero-β MHD model, which yields good agreement with the strongly inclined (non-radial) rise path of the filament. The same approach is used to reveal the process of magnetic twist release during a filament eruption.[112] Similarly, Guo et al.[34] studied another filament eruption using their zero-β MHD model with the initial condition of the magnetic field determined by an advanced flux rope insertion method that is based on regularized Biot-Savart laws. The flux rope insertion method can reconstruct the MFR reasonably well, even in a weak-field region for which the traditional NLFFF extrapolation codes often fail because of the large uncertainty of measurements in the vector magnetograms, but fine-tuning of the free parameters is often required to reach a solution consistent with the observed

Figure 3. Comparison of observation and MHD simulation of the sigmoid eruption associated with an X2.1 flare that occurred on September 6, 2011 The first two rows show the SDO/AIA observations at 304 and 171 Å, respectively, starting at 22:18 UT with a cadence of 2 min. The last two rows show the evolution of magnetic field lines in the MHD simulation with the same field of view as the observations. The time unit in the simulation is 20 s, and, thus, the cadence is also 2 min. The viewing angle in the top row is aligned with the SDO/AIA observations, whereas the bottom row shows a side view from the south. Image reproduced from Jiang et al.[101] with permissions from the AAS.

filament.[115–118] There are also a few studies[111,119–121] that use a non-force-free coronal field extrapolation[122–124] as the initial conditions of the MHD simulation, in which the eruption is directly triggered and likely driven by the initial unbalanced Lorentz force.

Some works also reconstruct a coronal magnetic field that is slightly farther away from being unstable and drive it to eruption using *ad hoc* ways that are not specified by the observed data. Inoue et al.[36,106,107] investigated the eruption mechanism of eruptive flares in the well-known AR NOAA 11158.[75] They first extrapolated NLFFF using SDO/HMI vector magnetogram observed for around 2 h before the flares, and found the NLFFF is stable in their zero-β MHD simulation. Then they applied enhanced anomalous resistivity to trigger tether-cutting recon-

nection[125] in the sheared arcades of the AR core, which eventually builds up a torus-unstable MFR to eruption. It is stressed[36] that, after the initiation phase, the eruption is mainly driven by the ongoing reconnection rather than TI, which explains why eruptions can still succeed even in a background field with a saddle-like profile of the decay index (i.e., the controlling parameter of TI with a value of around 1.5 as its threshold[84,126–129]), first with a TI-unstable and then a TI-stable area (Figure 4). With vector magnetograms provided by the Solar Optical Telescope (SOT[130]) onboard Hinode,[131] Amari et al.[73] modeled the eruption process of an X3.4 flare in AR NOAA 10930 by their Grad-Rubin-type NLFFF extrapolation code[132–134] and MHD simulation. First, a series of NLFFF extrapolations was performed to follow the quasi-static pre-flare evolution of the coronal field, in which an
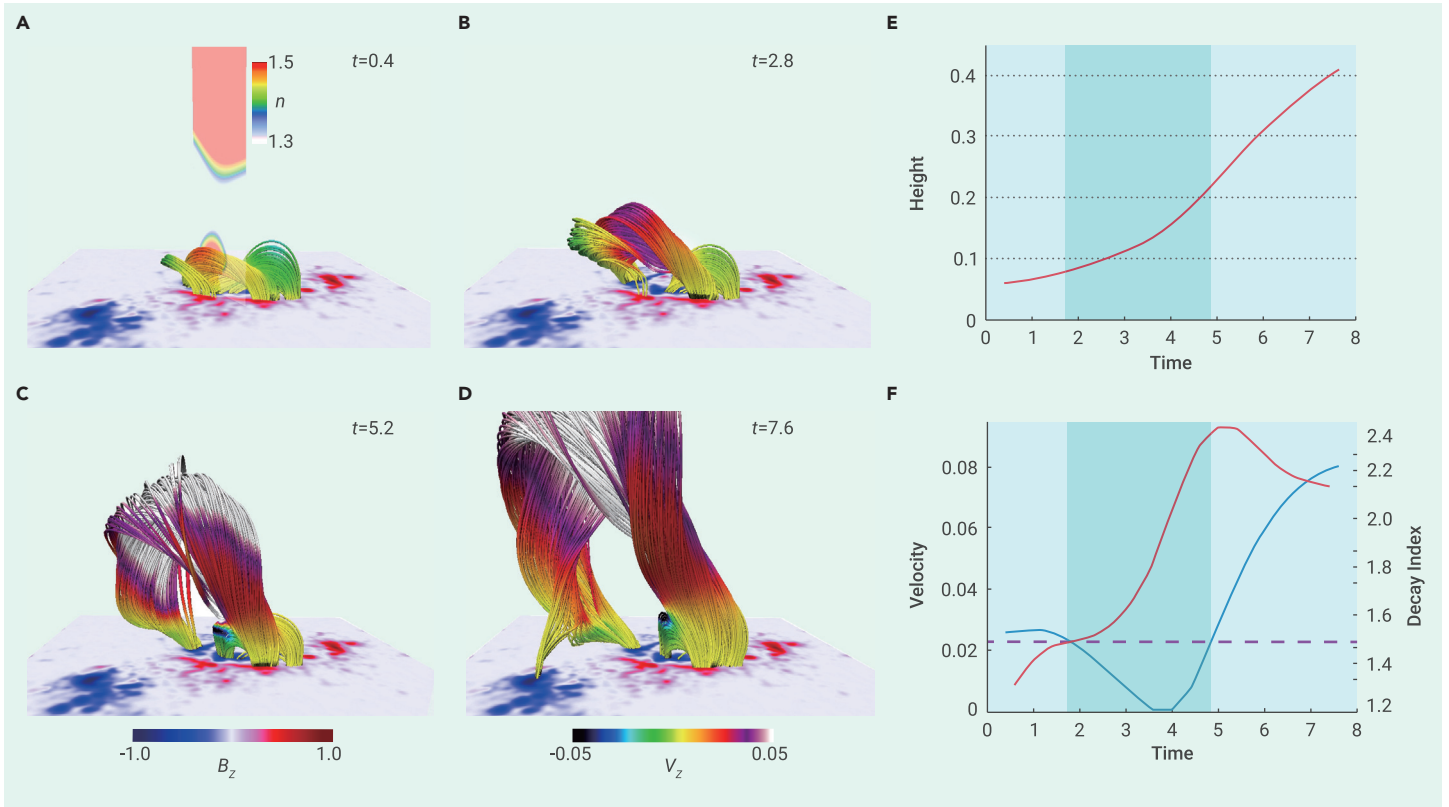
Figure 4. 3D dynamics of an eruptive flux rope in a zero-β MHD simulation for the M6.6-class flare of AR NOAA 11158 (A–D) Temporal evolution of the dynamics of the eruptive flux tube together with B_z distribution at the bottom surface. The color of the field lines corresponds to the vertical velocity component. The vertical cross section in (A) is shown with the decay index value of the overlying field. (E) Evolution of the apex of the axis of the erupting flux rope. (F) Evolution of the velocity (red line) and the decay index (blue line), measured at the axis apex of the flux rope (All quantities are expressed in non-dimensional values, and the physical units can be found in Inoue et al.[36]). The dashed line denotes the critical decay index of $n = 1.5$ (i.e., the threshold of TI), and the light-blue and blue masks mark regions $n > 1.5$ and $n < 1.5$, respectively. The flux rope can erupt successfully even with the decay index of a saddle-like profile. Image reproduced from Inoue et al.[36]

MFR is found to be formed gradually. Then the NLFFF based on the last available vector magnetogram, which is taken around 6 h before the flare is entered into the MHD model. Like the work of Inoue et al.,[106] the input NLFFF model is still stable and shows no eruption in the MHD model. Further stress of the coronal field through artificially specified converging flows on the boundary conditions, which mimics flux cancellation, is used to drive the MFR to approach an unstable state till its eruption. Using the same approach, Amari et al.[135] simulated the failed eruption of an MFR in the super AR NOAA 12192 (the largest AR in the last two solar cycles[136]), in which the so-called "magnetic cage" (i.e., the overlying strapping field lines) was found to play a key role, resulting in the unusual confined flares of X-classes in that AR.[137] The eruption of AR NOAA 10930 was also studied by Muhamad et al.,[138] who first extrapolated a stable NLFFF model for the pre-flare field and then let a small bipole emerge into the large-scale field with different orientations relative to the main PIL. They confirmed that the bipole field with a so-called opposite polarity and reversed shear structures can effectively trigger flare eruption, which was originally suggested by Kusano et al.[139]

With realistic simulations that are constrained or driven by observed data, significant insight into complex eruption events can be gained. By an advanced simulation based on their previous work,[101] Jiang et al.[140] demonstrated a three-stage magnetic reconnection scenario of the sigmoid eruption in AR NOAA 11283. These three reconnection episodes occurred successively in different locations in the corona and led to a complex process of CME formation. The initial sigmoidal flux rope breaks one of its legs, and quickly gives birth to a new tornado-like magnetic structure that is highly twisted and has multiple connections to the Sun at remote places from the original flare site. The final weak reconnection triggered in the newly formed current sheet associated with the relatively weak field that connects the remote polarity might provide a viable explanation for the EUV later phase of the flare.[141,142] Inoue et al.[37,108] simulated the X9.3 flare in AR NOAA 12673 and revealed a complex eruption process in which a series of small flux ropes straddled along the same PIL prior to the flare reconnect to form a large, highly twisted MFR that might trigger its eruption by kink instability.[143] The same event was also simulated by Jiang et al.,[109] who focused on accurately char-

acterizing the evolving magnetic topology during the eruption and were able to reproduce the spatial location and the temporal separation of the complex flare ribbons and the dynamic boundary of the erupting MFR's feet. The temporal profile of the total reconnection flux is comparable with the soft X-ray light curve. A recent ultra-high resolution, fully 3D MHD simulation[144] (reaching a spatial scale of 45 km) even reproduced the successive formation of mini flux ropes (i.e., plasmoids in 2D) in the reconnection of a confined flare that matches the high resolution from New Vacuum Solar Telescope (NVST)[145] and SDO, as shown in Figure 5.

Although with such success, the combination of static reconstruction for pre-eruptive field and time-dependent simulation of its subsequent eruption cannot self-consistently show how the pre-eruptive field is formed and how the eruption is triggered (but such simulations can be used to test the different scenarios). One of the issues is that many NLFFF models contain a numerical residual of Lorentz forces, which is often non-negligible, as indicated by the misalignment of the current density and magnetic field; thus, the initial magnetic field already deviates from a force-balanced state because of the numerical residual forces. For example, the current-weighted sine of the angle between J and B for many NLFFF models is typically in the range of 0.2–0.4.[147–150] Such residual force can instantly induce plasma motions in a low-β and highly tenuous plasma environment. This motion provides a perturbation to trigger instability and, thus, eruption of the magnetic field if it is unstable or not far from unstable. But there is also the possibility that the large residual force may overtake the instability, and, thus, the true initiation mechanism of eruption may not be identified. So, it is more promising when the NLFFF can be relaxed to a well-established equilibrium by cleaning the residual forces and to use this equilibrium as the initial conditions of MHD simulation. Although there are some studies[73,106] beginning simulation from a stable NLFFF, they need to artificially drive the field to evolve toward eruption by *ad hoc* boundary flows or enhanced resistivity. In this case, it is generally not guaranteed that the resulted evolving magnetic field at the bottom boundary will match the evolution of the observed magnetogram. In other words, the self-consistent evolution of the coronal field from a stable equilibrium to eruption matching the variation in the photospheric field is still out of reach.
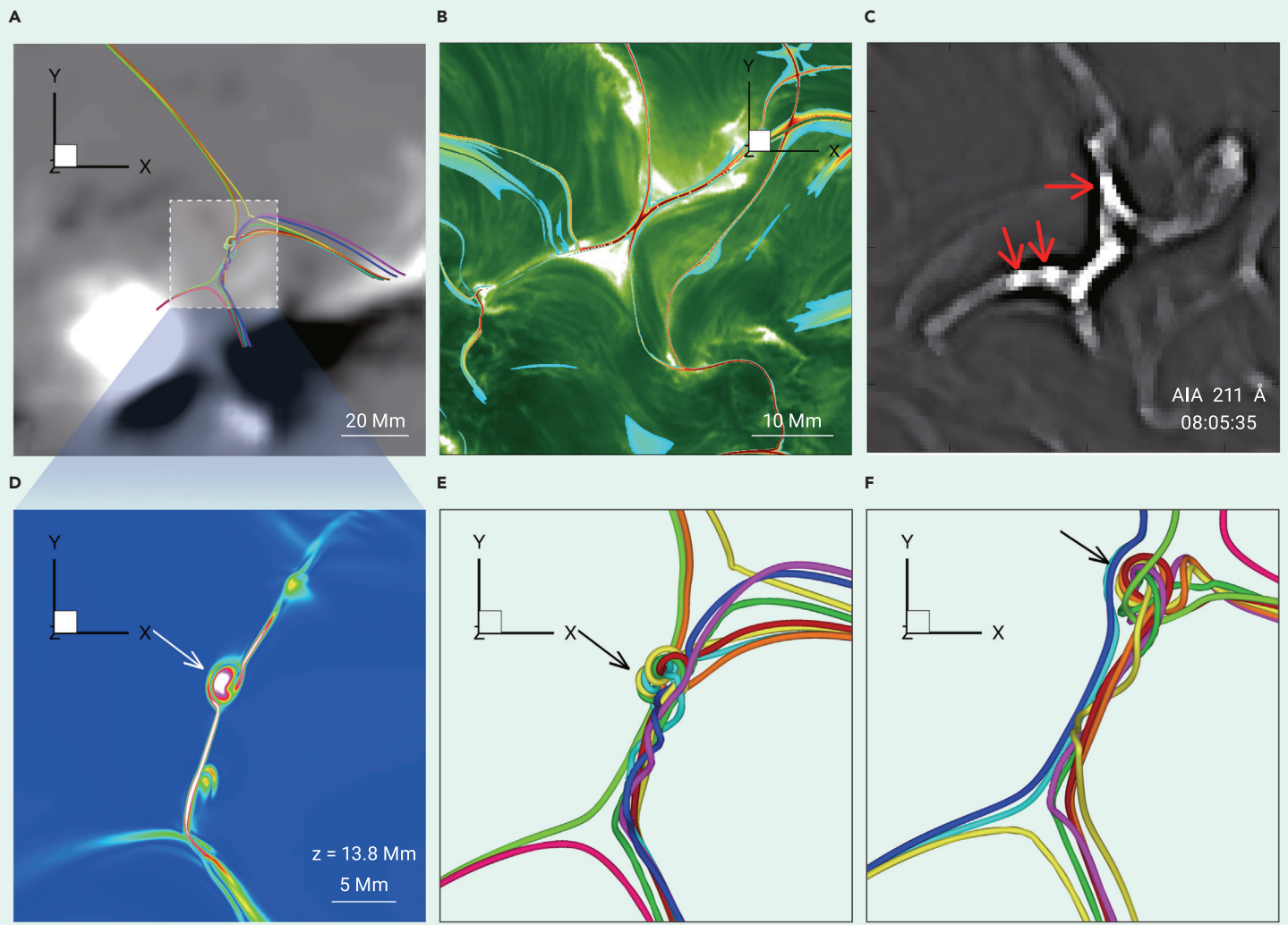
Figure 5. High-resolution observation and data-driven modeling of a confined flare, revealing fast plasmoid-mediated reconnection (A) Large-scale structure of the magnetic field lines (colored lines) involved in the flare reconnection. The background image shows the distribution of the photospheric magnetic flux density B_z. (B) NVST Hα image of the flare site, which shows that filament threads of opposite sides approach each other, form an X shape, and reconnect, resulting in chromospheric brightening. Superimposed is a horizontal map of the separatrices or quasi-separatrix layers (QSLs[146]) (with $\log_{10} Q > 2.5$, where Q is the magnetic squashing degree and quantifies the gradient of magnetic field-line mapping with respect to their footpoints) calculated from the pre-flare magnetic field data. (C) SDO/AIA 211 Å image of the flare plasma in the corona. The bright blobs as denoted by the red arrows are manifestations of plasmoids generated repeatedly from the flare current sheet. (D) Distribution of the electric current density in the current sheet in the data-driven simulation. (E and F) The corresponding magnetic structure of the current sheet at two different times, showing the formation and movement of the 3D magnetic structure of the plasmoids; i.e., mini flux ropes. The arrows indicate the evolution of the biggest plasmoid as generated in the current sheet, moving northward to the separatrix. Image reproduced from Yan et al.[144]

DATA-DRIVEN SIMULATION OF QUASI-STATIC EVOLUTION TO ERUPTION

A self-consistent, data-driven model of solar eruptions should be able to simulate the coronal magnetic field following a long-duration, quasi-static evolution all the way to its fast eruption. Jiang et al.[44] developed such an MHD model (the so-called driven ARE (DARE)-MHD model[44,151,152]) and successfully simulated a flux emergence event of over 3 days that finally leads to an eruption (of an M-class flare with a CME) in the topology-complex AR NOAA 11283. The simulation is started with a potential field extrapolation from the vertical component of the magnetogram taken for the initial time; thus, one can see how the pre-flare magnetic free energy is accumulated continually from the very beginning, driven by the flux injection with a strong shearing motion. The simulated field morphology well resembles the AIA observations for the whole process. The timing of the simulated eruption onset matches the observed flare time within an offset of less than 2 h (by comparing it with the whole simulation of 3 days), which supports the model capturing the key transition of dynamics from pre-eruption to eruption. By a thorough analysis of the magnetic topology evolution, Jiang et al.[44] concluded that the flux emergence leads to formation of a jet-like configuration that is favorable for a self-amplifying reconnection between the newly emerged non-potential arcade and the pre-existing open flux, which is subsequently triggered and results in the eruption (Figure 6). This scenario is actually similar to the breakout model.[96]

In this event, no MFR formed, but while studying another event, the DARE-MHD simulation supports the high-resolution observations by the Goode Solar Telescope[153] and SDO of flux emergence of a small-scale MFR and its subsequent eruption.[154] Similar simulations of the large-scale MFR formation and eruption have been carried out for CME initiation in AR NOAA 12371.[46,151]

The DARE-MHD model has also been used to study confined flares. For instance, Jiang et al.[152] simulated a 2-day magnetic evolution that lead to the X3.1 confined flare in the super AR NOAA 12192. They showed that a thin layer of intense current is formed gradually in the AR's core. The current layer was successively enhanced, driven by the photospheric shearing motion, until it became so thin (as a current sheet) that a tether-cutting reconnection[125] between the sheared magnetic arcades sets in, which is responsible for the flaring process, and after the reconnection, the current is substantially dissipated. Comparison with the AIA observations shows that the footpoints of the newly reconnected field lines reproduced almost exactly the location of the flare ribbons, and the morphology of the reconnecting field lines and the simulated EUV image (using a similar method as proposed by Cheung and DeRosa[23]) well resembles the flaring loops. According to the simulation, this flare failed to erupt as a CME because the consequence of the reconnection is still a sheared arcade without forming an escaping MFR because the pre-flare field is only weakly twisted,[155] but of course the strong overlying field also plays an important role.[135,137]
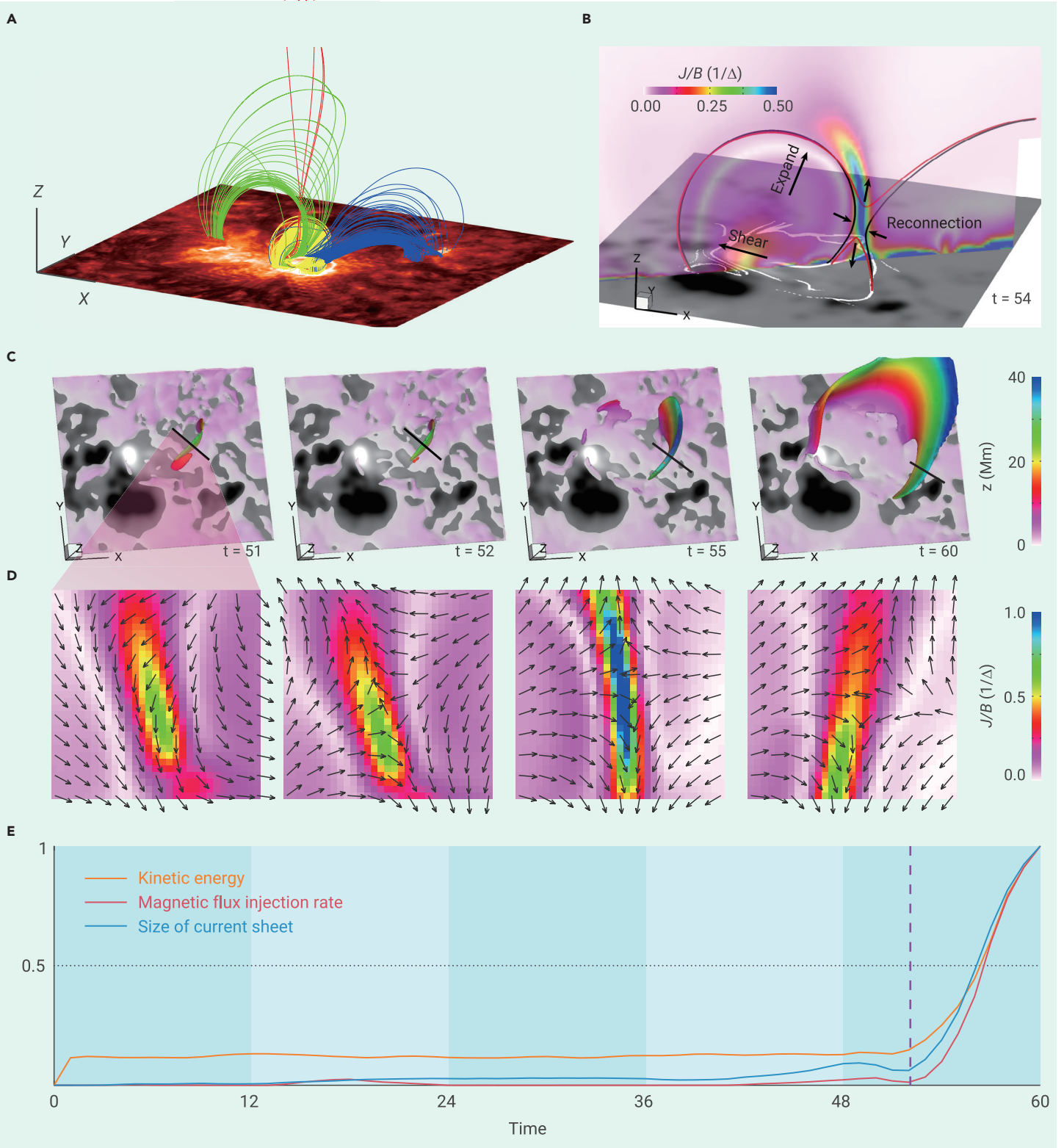
Figure 6. The initiation mechanism of an M-class flare and eruption as revealed by a data-driven full MHD simulation (A) Sampled field lines showing the basic topology at the flare onset. Shown at the bottom is a AIA 304-Å image taken near the flare peak time to show the flare ribbons. The image has a field of view of 400 × 300 Mm². The locations of flare ribbons are matched well by the footpoints of the reconnecting field lines. (B) Illustration of the jet-like reconnection as an eruption trigger mechanism. The bottom surface shows the map of B_Z overlaid by white lines showing the trace of the separatrix and QSL ($\log_{10} Q > 5$). This image is an enlarged view of the flare core site with field of view of about 100² Mm². (C and D) Current sheet development and magnetic reconnection. The field of view is the same as in (B). (E) Evolution of the size of the current sheet and reconnection magnetic flux injection rate compared with that of the kinetic energy. All of these quantities are scaled by their values at $t = 60$, and the time unit is 90 s. Image reproduced from Jiang et al.[44]

Recently, efforts have been made to compare the simulated eruption with the observed features more quantitively. For example, Guo et al.[35] simulated a short-time evolution of about 1 h before a small flare (C4.7) to its onset in AR NOAA 11123 using their data-driven zero-β MHD model and reproduced an MFR erup-

tion with a morphology highly consistent with the corresponding AIA observations of the flare-associated filament eruption (Figure 7). A detailed analysis of the kinematics of the rise of the MFR showed that the simulated eruption distinctly demonstrates a two-stage evolution similar to the slow-rise
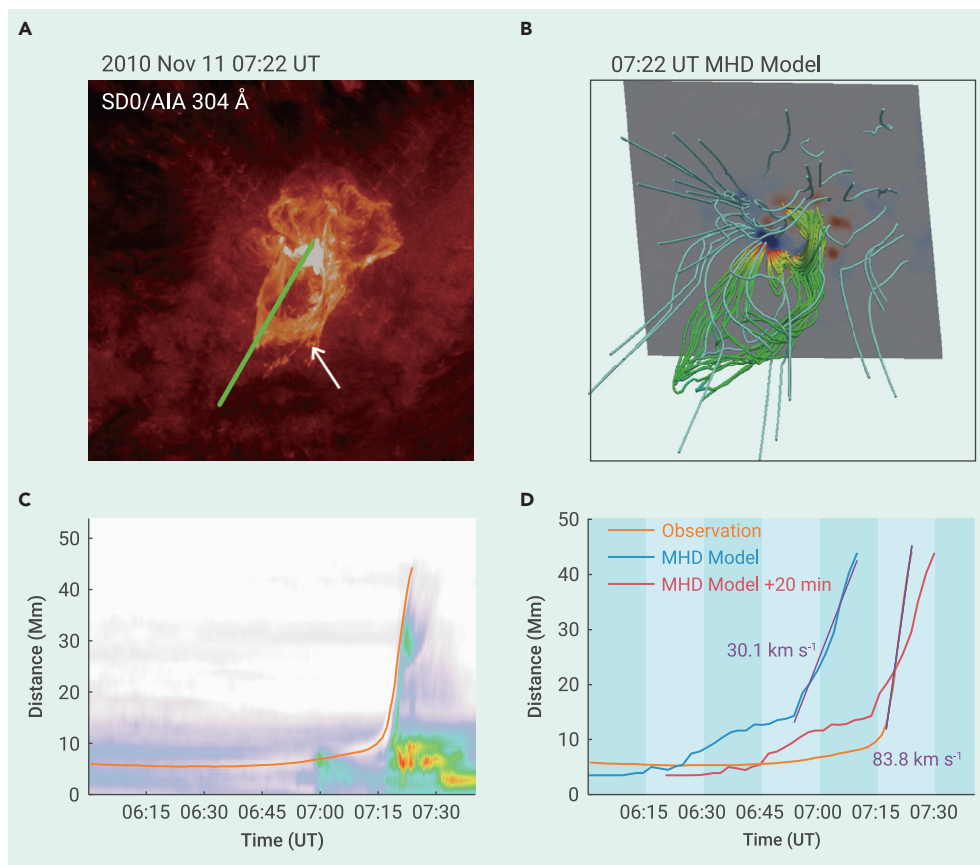
Figure 7. Comparison of observation and data-driven zero-β MHD simulation of the filament eruption in AR NOAA 11123 on November 11, 2010 (A) SDO/AIA 304-Å image of the filament eruption. The green solid line indicates the slice that is selected to measure the time-distance profile of the erupting filament in the bottom panels. The white arrow indicates the erupting filament material. (B) Magnetic field lines of the MHD model. (C) Time-distance measurement of the erupting filament. (D) Time-distance profiles measured in the 304-Å observations and the MHD simulation. The blue curve indicates the flux rope front in the original simulation, and red curve shows the same result but with time being shifted by 20 min later. The two straight lines are the linear fits to the rapid eruption stage of the flux rope. Image reproduced from Guo et al.[35] with permissions from the AAS.

Moreover, by recovering a continual evolution that allows a "memory" of magnetic topology and build-up of electric currents and free magnetic energy, data-driven models maintain a high degree of self-consistence compared with other models. Data-driven modeling helps us to find the key mechanism that initiates the eruptions and reveal more in depth the physical behaviors of eruption that challenge theoretical and idealized models, which has greatly extended our understanding of the coronal magnetic dynamics. Although different eruption scenarios can be tested with simulations of other types, only data-driven simulations can be used to identify the actual scenario in real events. For example, many NLFFF analyses[84,157–160] of coronal fields show pre-flare MFR, suggesting that the MHD instabilities of the MFR could trigger the eruption (by studying the twist number and decay index), but only data-driven MHD simulations can determine whether these instabilities exist and their role in producing eruptions. Some unexpected results have already been found. For instance, a Lorentz force component resulting from an MFR's radial magnetic field could result in failure of the MFR to erupt, which is not considered in the theory of TI. Another finding is that, when reconnection begins, the eruption is mainly driven by the ongoing reconnection rather than TI, which explains why eruptions can still succeed in a background field with a saddle-like profile of the decay index.

Next we provide a summary of future developments and applications of these models.

and fast-rise phases of many observed eruptions;[156] by computing the decay index, they suggested that the slow rise to fast eruption is likely due to TI. Using the same model, Zhong et al.[39] showed the capability of simulating a failed eruption that occurred on January 30, 2015. Similarly, their zero-β model is initialized with an NLFFF extrapolated for a short time of half an hour before flare onset and successfully recreated the initial rise of an MFR (likely because of kink instability) and then its confinement in a complex magnetic topology. They calculated the footprints of evolving quasi-separatrix layers (QSLs[146]) during the flare reconnection, which are found to coincide rather well with the structure and evolution of the observed flare ribbons. By careful analysis of different components of the Lorentz force (Figure 8), they revealed for the first time that a particular component, resulting from the MFR's radial magnetic field, which is defined in the local cylindrical coordinates of the MFR and is related to the non-axisymmetry of the MFR's cross-section, essentially constrains the erupting MFR. This differs from the prediction of TI, in which the major confining force should come from the external strapping field, and such new results demonstrate that a data-driven model can disclose the complexity of physics in a realistic eruption that has not been considered in traditional theories. The data-driven model has also been shown to be able to simulate successive eruptions from the same region.[38]

SUMMARY AND OUTLOOK

To summarize, major developments of data-driven modeling of coronal magnetic fields have been witnessed over the last 10 years. A variety of models have been proposed, with different assumptions and implementations of the controlling equations, the numerical solver, as well as the initial and boundary conditions to drive the models. These models have been applied to simulation of the long-term evolution and fast eruptions of complex coronal magnetic fields with various topologies. The results have well demonstrated that data-driven simulations are able to achieve an unprecedented high degree of realism exceeding non-data-driven simulations, in particular by reproducing the eruption process with a complexity that is beyond the scope of idealized or theoretical models. This has been shown by the striking resemblance of the magnetic topology in the simulated eruptions with the observed erupting coronal loops and filaments as well as the complex morphology and evolution of the flare ribbons.

Joint assessment of different codes

As in the case of NLFFF extrapolation, for which a variety of codes exist and joint testing of these codes is important to guide code improvements,[147,149,161] different data-driven models should also be compared jointly; for example, using some ground-truth datasets (but of course from other types of simulations). Such a comparative study can help to identify the key factors that make performance of the various models different. Toriumi et al.[162] first examined four different data-driven models[23,35,43,44] using data from an idealized flux emergence simulation (FES) of a twisted magnetic flux tube emerging from the convection zone into the corona. The photospheric magnetic and velocity fields produced by the FES are input to drive the different data-driven models as part of their bottom boundaries. It was found that, although all of these data-driven models successfully reproduced a flux rope structure, the quantitative discrepancies are considerable. Even though some of the models can reproduce the magnetic field energy and relative helicity in the corona quite well, the 3D magnetic configuration is still rather different from the ground-truth data (see Figures 4 and 5 in Toriumi et al.[162]). The discrepancies among the models were attributed mainly to the highly non-force-free input photospheric field and the modeling constraints, such as the treatment of background atmosphere, the bottom boundary setting, etc.

Indeed, in a following work, Jiang and Toriumi[163] tested the DARE-MHD model with the bottom boundary driven by three sets of data from the same FES sliced at incremental heights, which correspond to the photosphere, the chromosphere,
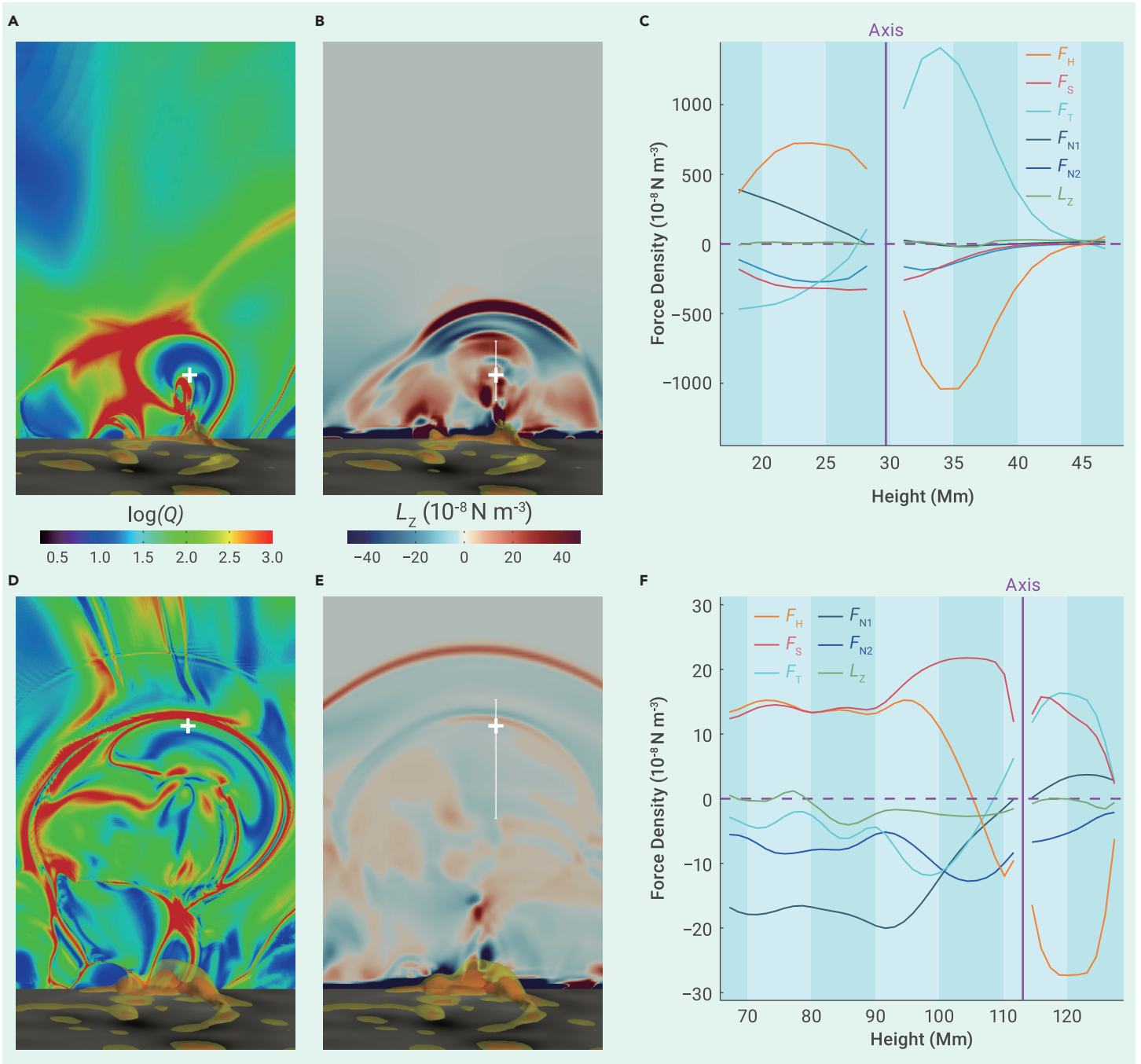
Figure 8. A detailed analysis of different components of the Lorentz force for a failed eruption as reproduced by a data-driven MHD simulation (A–F) The early phase (A–C) and later phase (D–F) of the eruption. (A and D) Distribution of the QSLs in the central cross-section, which can outline the boundary of the erupting MFR. The location of the MFR axis is denoted by a white plus symbol. (B) and (E) Distribution of the vertical component of the Lorentz force, L_z. (C) and (F) Distribution of L_z along the white line in (B) and (E), respectively. The gray line represents the net force. The orange, purple, blue, red, and cyan lines represent the different components, including the hoop force (F_H), non-axisymmetry induced forces (F_{N1} and F_{N2}), strapping force (F_S), and tension force (F_T). The black vertical line indicates the location of the axis of the MFR. F_{N1} changes its direction during the eruption process. It is initially upward but becomes downward in the end, constraining the MFR eruption. Image reproduced from Zhong et al.[39]

and the base of the corona, respectively. They first compared the relative magnitudes of the Lorentz force contained in these datasets using the ratio of the integrated Lorentz force (and torque) to the integrated magnetic pressure gradient force (and its torque). This ratio, or normalized force (and torque), for a perfectly force-free magnetogram is 0 (a criterion of below 0.1 is commonly accepted to be force free[164–166]), whereas, for an extremely non-force-free field, it is close to 1, meaning that the magnetic pressure force and the tension force are so unbalanced that the net Lorentz force is comparable with one of its components, the total magnetic pressure force. As found by Jiang and Toriumi[163], for the photospheric data of the FES, the ratio (for force and torque) is close to 1 in the whole time evolution, meaning that the photosphere data have a very strong Lorentz force. For the data sliced at two higher levels, the normalized Lorentz force and

torque in the early phase of emergence are still large (close to 1), but decrease substantially (to around 0.2) with emergence of the magnetic flux, indicating that, at these levels, the fields are relaxing to a more force-free state. As a result, the DARE-MHD using the photosphere data fails to reproduce the coronal magnetic field, whereas at the two higher levels above the photosphere, the DARE-MHD yields results in much better agreement with the FES. This confirms that the Lorentz force in the boundary data is a key issue affecting the results of the DARE-MHD model, and the key reason is that the bottom surface in the DARE-MHD model (and in many other models) is assumed to be the coronal base with a plasma number density of around 10^9 cm^{-3}, which is many orders of magnitude smaller than that of the photosphere (about 10^{17} cm^{-3}). Thus, if the strongly forced photospheric magnetic field is entered into a model that uses typical

settings for the atmosphere in the corona, such a strong Lorentz force cannot be balanced by the tenuous plasma. It can induce largely spurious plasma motions, which, in turn, amplify the magnetic field by the magnetic induction equation and could make the evolution run away.[162,163] The other two data-driven MHD models, developed by Guo et al.[35] and Hayashi et al.[43] and examined by Toriumi et al.,[162] use much denser plasma (with a number density of 10^{13} cm^{-3} and 10^{17} cm^{-3}, respectively) at the lower boundary and can avoid such an inconsistency (by keeping the induced motions at a reasonable level of speed). This emphasizes the need for incorporating a more realistic atmospheric stratification from the photosphere, chromosphere, and transition region to the corona (if the photosphere magnetic field is the only data that can be used). With this, the data-driven model can also be used to probe the physical mechanisms behind the reverse feedback of coronal eruption to the photosphere; for example, the rapid, permanent change of photospheric magnetic fields as often observed through flares[167,168] and the sudden reversal of rotation in a sunspot during a solar flare.[169,170]

On the other hand, the observed photospheric field for flux-emerging ARs from SDO/HMI has been found to be much closer to force free than the FES data, as demonstrated recently by Duan et al.[171] They conducted a statistical study of the normalized Lorentz forces and torques with a substantially large sample of 3,536 vector magnetograms from 51 ARs taken by SDO/HMI over the period of 2010–2019. These ARs were selected as having significant flux emergence during their passage on the solar disk within ± 45° in longitude from the Sun's central meridian. The normalized Lorentz forces and torques for all vector magnetograms are, on average, very close to 0.1, which is much smaller than that from the simplified FES. Thus, on one hand, in future investigations, one should consider using realistic convective FES models that could yield more relaxed emergence[172,173] as the ground-truth data to perform a more insightful assessment of the different data-driven models. Or, in comparison with other data-driven models, the models that include the atmosphere of only the corona should be provided with magnetic field data in the higher and more force-free solar atmosphere, especially considering that some of these models adopt an NLFFF as the initial condition. On the other hand, such an inconsistency, as found by the FES and the observed magnetogram (i.e., the latter is much more closer to force free than the former) calls for more realistic flux emergence models[174] and even solar dynamo models[175] with constraint from the observed photospheric magnetic field.

Coupling of local and global models

Currently, most of the data-driven models for eruptions are implemented in a local Cartesian box, which, unavoidably, has numerical boundaries at the side and top of the computational volume, and it has long been a big problem to specify the conditions on these boundaries so that they can be numerically stable and non-reflecting. To avoid this difficulty, many modelers choose to simply fix the variables on the numerical boundaries and stop their simulation before the disturbance induced by eruption reaches these boundaries.[35,39,109] There are also models using periodic conditions for the side boundaries, which, however, may result in unreasonably distorted structures of the simulated magnetic field and plasma.[176] Future data-driven simulations of eruptions need to be extended to the global corona and incorporate solar wind by utilizing full-disk vector magnetograms (rather than only LOS synoptic maps) to study how an initiated CME evolves and interacts with the large-scale structures in the local corona and in the interplanetary space. This, on one hand, can avoid the sub-Alfvénic numerical boundaries, and more importantly, on the other hand, can provide a more realistic evolution of CME in the heliosphere than most current simulations of CME propagations that commonly employ an artificially inserted, force-unbalanced MFR in the corona to generate an eruption[177–181] and will definitely be a big step forward for developing sophisticated model of space weather, which is driven by solar eruptions. By coupling the local and global models, it is also important to examine whether the eruptive structure (e.g., flux rope) formed in the local frame is confined or has access to outer space. For instance, DeRosa and Barnes[182] surveyed the large-scale magnetic flux overlying the ARs of a number of X-class flares (including eruptive and confined ones) using the potential field source surface (PFSS) model.[15] They found that, in general, the ARs of eruptive events are located closer to the open flux than those of confined ones. These kinds of studies using data-driven models may provide important insights into how the eruptive structures interact with the different background fields and result in successful or failed eruptions. A few efforts have already been made to develop such coupled models. For example, Wu et al.[183] entered the eruptive magnetic structure of AR NOAA 11283

obtained from Jiang et al.[101] into a global coronal and solar wind model to track the propagation of the eruption. Hayashi et al.[184] used the output from the magnetofrictional model (spherical version) of Cheung and DeRosa[23] to specify the inner boundary conditions of their global heliosphere model and simulated an eruption from AR NOAA 11158. More quantitative comparisons between the simulation results with coronagraph observations and in-situ data within the corona are required; for example, from the Parker Solar Probe[185,186] and Solar Orbiter,[187] to validate and constrain the data-driven models.

At the other end of the spectrum, data-driven MHD simulations for eruptions should also be coupled with very small-scale photospheric magnetic field evolutions, as observed with very high spatial resolution but in a small field of view. This is because there are small-scale processes playing key roles in producing eruptions. For example, some high-resolution observations[188,189] show that the emergence of very-small-scale magnetic flux reversed to the large-scale field of a pre-existing sheared arcade, the so-called reversed magnetic shear mechanism,[139,188] could lead to a global eruption, and this mechanism has yet to be investigated by data-driven modeling. Another example is magnetic flux cancellation, in which small-scale magnetic flux elements of opposite polarities meet at the PIL and cancel each other; this is believed to be a key mechanism of building up pre-eruption coronal MFRs. Because the nature of flux cancellation is still elusive, this needs to be carefully studied with data-driven simulations driven by high-resolution data focusing on the small-scale magnetic structures near the PIL. High-spatial-resolution vector magnetograms obtained by, e.g., the Daniel K. Inouye Solar Telescope (DKIST[190]), could provide boundary data for such small-scale MHD simulations. High-temporal-resolution data are also indispensable for simulating fast flux emergence events.[72] In addition to the spatial resolution and temporal cadence, vector magnetic fields also have to be accurate enough to maintain the credibility of data-driven simulations. Vector magnetic field observations often suffer from two major problems, 180° ambiguity and the relatively low accuracy of the transverse component compared with the LOS component. Significant progress to resolve these problems was made by launching the Solar Orbiter.[187] The combination of vector magnetic field observations from two perspectives, such as SDO and Solar Orbiter, could resolve the 180° ambiguity[191] and increase the precision of their transverse components.

Including more physics

Most data-driven models as discussed are focused on magnetic fields, whereas the plasma is not dealt with realistically (either for initial conditions or in model equations), especially in the magnetofrictional and the zero-β models. By discarding the thermal pressure, these simplified models might fail when there is a fast reconnection in the field, where thermal pressure could play an important role in the dynamics in the weak-field region of magnetic field dissipation. Further improvements should be devoted more to the full MHD and even the radiative MHD models. On the one hand, more physics need to be included in the energy equation by considering the effects of coronal heating, thermal conduction, and radiative cooling. On the other hand, more realistic initial and boundary conditions are required to be used for not only the magnetic field but also the plasma density and temperature, which, for example, could be determined using differential emission measure tomography.[192] With these advancements, the models can obtain the capability to simulate the wealth of emission structures (such as EUV coronal loops, filaments, and flare emissions) of the coronal field that can be directly compared with observations, which, in turn, gives more constrains to the models.

Achieving higher accuracy of computation

The value of numerical resistivity is also a problem for modeling magnetic reconnection. Currently, most data-driven models have numerical resistivity with values much higher by orders of magnitude than the realistic coronal value, and, thus, slow reconnection is often triggered too easily; in other words, the current layer cannot be sufficiently thin to let a fast reconnection set in. For example, a recent simulation[97] shows that the magnitude of resistivity can substantially affect the result of eruption-initiation simulations, which is associated with a long-standing question regarding the initiation of eruptions. It has been well established by many MHD simulations[193–195] in two dimensions (or translationally invariant geometries) with high accuracy that a magnetic arcade sheared continuously will asymptotically approach an open field[196,197] containing a thin current sheet, and the system experiences a global eruption when reconnection sets in at

the current sheet. However, this simple and efficient scenario of eruption initiation has never been reproduced in fully 3D MHD simulations with sufficiently high accuracy until recently by Jiang et al.,[97] and the key reason why previous 3D simulations failed is that their models have an unreasonably large resistivity (in the line-tied bottom boundary, the computational volume, or both) so that the thin current sheet cannot form (because the current layer dissipates quickly by the large resistivity). Therefore, future data-driven models should consider improving numerical accuracy and resolution to reach a sufficiently small resistivity and, eventually, to bridge the gap between the numerical Lundquist number of only a few $10^2 \sim 10^3$ to a realistic one of around 10^{13}.

Improving computational efficiency

A major limitation for application of data-driven comprehensive models that should include all aforementioned improvements is the large amount of computing resources required. According to the authors' experience, to simulate the evolution of a typical size AR (say, 300 Mm in all three directions) for a typical timescale of a few days with a grid resolution that matches the HMI data (720 km), an MHD model with isothermal simplification needs months of computing time even when parallelized with a medium number of CPUs (for example, 100 processors with a frequency of 3 GHz). To reduce the computing time, some modelers[44,151,152] chose to speed up the cadence of feeding the observed data into the model by tens of times. This is reasonable by taking advantage of the fact that the photospheric evolution speed (with a typical velocity of $0.1-1$ km s^{-1}) is slower than the coronal evolution speed (of a few Mm s^{-1}) by about three orders of magnitude. Speeding up the driving process is also necessary, considering that the numerical resistivity is much larger than the realistic one, and, thus, the global diffusion speed of the free magnetic energy could be faster than the energy injection rate from the bottom boundary when using the realistic timing of driving. In this case, no free energy (and current) can be accumulated in the corona, and no eruption can be initiated. Although speeding up photospheric driving can be acceptable in the non-eruptive time duration, the coronal magnetic field may still not relax sufficiently to reproduce the quasi-static evolution in the real corona, while during eruptions, it may not be consistent with the sped-up evolution of the photospheric field. Therefore, solving all these problems demands more accurate numerical solving of the controlling equations and faster computing techniques developed for hardware (for example, using GPU computing) and software. The next generation of data-driven modeling should be efficient enough to match the fast-developing observation capability and eventually have computing power faster than real time and an accuracy high enough for prediction of solar eruptions and for use as a key module for space weather forecasting.

REFERENCES

1. Aschwanden, M.J. (2004). Physics of the Solar Corona. An Introduction (Springer Praxis Books).
2. Chen, P.F. (2011). Coronal mass ejections: models and their observational basis. Living Rev. Solar Phys. **8**, 1.
3. Shibata, K., and Magara, T. (2011). Solar flares: magnetohydrodynamic processes. Living Rev. Solar Phys. **8**, 6.
4. Howard, T. (2011). Coronal Mass Ejections. Astrophysics and Space Science Library, **376** (New York: Springer).
5. Solanki, S.K., Inhester, B., and Schüssler, M. (2006). The solar magnetic field. Rep. Prog. Phys. **69**, 563–668.
6. Lin, H., Kuhn, J.R., and Coulter, R. (2004). Coronal magnetic field measurements. Astrophys. J. **613**, L177–L180.
7. Chen, B., Shen, C., Gary, D.E., et al. (2020). Measurement of magnetic field and relativistic electrons along a solar flare current sheet. Nat. Astron. **4**, 1140–1147.
8. Fleishman, G.D., Gary, D.E., Chen, B., et al. (2020). Decay of the coronal magnetic field can release sufficient energy to power a solar flare. Science **367**, 278–280.
9. Gary, D.E., and Hurford, G.J. (1994). Coronal temperature, density, and magnetic field maps of a solar acitve region using the Owens Valley Solar Array. Astrophys. J. **420**, 903.
10. Van Doorsselaere, T., Nakariakov, V.M., Young, P.R., and Verwichte, E. (2008). Coronal magnetic field measurement using loop oscillations observed by Hinode/EIS. Astron. Astrophys. **487**, L17–L20.
11. Yang, Z., Tian, H., Tomczyk, S., et al. (2020). Mapping the magnetic field in the solar corona through magnetoseismology. Sci. China Technol. Sci. **63**, 2357–2368.
12. Yang, Z., Bethge, C., Tian, H., et al. (2020). Global maps of the magnetic field in the solar corona. Science **369**, 694–697.
13. Si, R., Brage, T., Li, W., et al. (2020). A first spectroscopic measurement of the magnetic-field strength for an active region of the solar corona. Astrophys. J. **898**, L34.
14. Landi, E., Hutton, R., Brage, T., and Li, W. (2020). Hinode/EIS measurements of active-region magnetic fields. Astrophys. J. **904**, 87.
15. Altschuler, M.D., and Newkirk, G. (1969). Magnetic fields and the structure of the solar corona: I: methods of calculating coronal fields. Solar Phys. **9**, 131–149.
16. Guo, Y., Cheng, X., and Ding, M. (2017). Origin and structures of solar eruptions II: magnetic modeling. Sci. China Earth Sci. **60**, 1408–1439.
17. Régnier, S. (2013). Magnetic field extrapolations into the corona: success and future improvements. Solar Phys. **288**, 481–505.
18. Wiegelmann, T. (2008). Nonlinear force-free modeling of the solar coronal magnetic field: coronal magnetic fields. J. Geophys. Res. **113**, 1–19.
19. Wiegelmann, T., and Sakurai, T. (2021). Solar force-free magnetic fields. Living Rev. Solar Phys. **18**, 1.
20. Priest, E.R. (1984). Solar Magneto-Hydrodynamics (D. Reidel Pub. Co.).
21. Priest, E.R. (2013). Magnetohydrodynamics of the Sun (Cambridge University Press).
22. Cheung, M.C.M., Pontieu, B.D., Tarbell, T.D., et al. (2015). Homologous helical jets: observations by IRIS, SDO, and Hinode and magnetic modeling with data-driven simulations. Astrophys. J. **801**, 83.
23. Cheung, M.C.M., and DeRosa, M.L. (2012). A method for data-driven simulations of evolving solar active regions. Astrophys. J. **757**, 147.
24. Gibb, G.P.S., Mackay, D.H., Green, L.M., and Meyer, K.A. (2014). Simulating the formation of a sigmoidal flux rope in AR 10977 from SOHO/MDI magnetograms. Astrophys. J. **782**, 71.
25. Kilpua, E.K.J., Pomoell, J., Price, D., et al. (2021). Estimating the magnetic structure of an erupting CME flux rope from AR12158 using data-driven modeling. Front. Astron. Space Sci. **8**, 631582.
26. Mackay, D.H., Green, L.M., and van Ballegooijen, A. (2011). Modeling the dispersal of an active region: quantifying energy input into the corona. Astrophys. J. **729**, 97.
27. Pomoell, J., Lumme, E., and Kilpua, E. (2019). Time-dependent data-driven modeling of active region evolution using energy-optimized photospheric electric fields. Solar Phys. **294**, 41.
28. Price, D.J., Pomoell, J., Lumme, E., and Kilpua, E.K.J. (2019). Time-dependent data-driven coronal simulations of AR 12673 from emergence to eruption. Astron. Astrophys. **628**, A114.
29. Price, D.J., Pomoell, J., and Kilpua, E.K.J. (2020). Exploring the coronal evolution of AR 12473 using time-dependent, data-driven magnetofrictional modelling. Astron. Astrophys. **644**, A28.
30. Weinzierl, M., Yeates, A.R., Mackay, et al. (2016). A new technique for the photospheric driving of non-potential solar coronal magnetic field simulations. Astrophys. J. **823**, 55.
31. Weinzierl, M., Mackay, D.H., Yeates, A.R., and Pevtsov, A.A. (2016). The possible impact of L5 magnetograms on non-potential solar coronal magnetic field simulations. Astrophys. J. **828**, 102.
32. Yardley, S.L., Mackay, D.H., and Green, L.M. (2018). Simulating the coronal evolution of AR 11437 using SDO/HMI magnetograms. Astrophys. J. **852**, 82.
33. Yardley, S.L., Mackay, D.H., and Green, L.M. (2021). Simulating the coronal evolution of bipolar active regions to investigate the formation of flux ropes. Solar Phys. **296**, 10.
34. Guo, Y., Zhong, Z., Ding, M., et al. (2021). Data-constrained magnetohydrodynamic simulation of a long-duration eruptive flare. Astrophys. J. **919**, 39.
35. Guo, Y., Xia, C., Keppens, R., et al. (2019). Solar magnetic flux rope eruption simulated by a data-driven magnetohydrodynamic model. Astrophys. J. **870**, L21.
36. Inoue, S., Kusano, K., Büchner, J., and Skála, J. (2018). Formation and dynamics of a solar eruptive flux tube. Nat. Commun. **9**, 174.
37. Inoue, S., Shiota, D., Bamba, Y., and Park, S.-H. (2018). Magnetohydrodynamic modeling of a solar eruption associated with an X9.3 flare observed in the active region 12673. Astrophys. J. **867**, 83.
38. Kaneko, T., Park, S.-H., and Kusano, K. (2021). Data-driven MHD simulation of successive solar plasma eruptions. Astrophys. J. **909**, 155.
39. Zhong, Z., Guo, Y., and Ding, M.D. (2021). The role of non-axisymmetry of magnetic flux rope in constraining solar eruptions. Nat. Commun. **12**, 2734.
40. Fan, Y.L., Wang, H.N., He, H., and Zhu, X.S. (2011). Study of the poynting flux in active region 10930 using data-driven magnetohydrodynamic simulation. Astrophys. J. **737**, 39.
41. Feng, X., Jiang, C., Xiang, C., et al. (2012). A data-driven model for the global coronal evolution. Astrophys. J. **758**, 62.
42. Galsgaard, K., Madjarska, M.S., Vanninathan, K., et al. (2015). Active region upflows: II. data driven magnetohydrodynamic modelling. Astron. Astrophys. **584**, A39.
43. Hayashi, K., Feng, X., Xiong, M., and Jiang, C. (2019). Magnetohydrodynamic simulations for solar active regions using time-series data of surface plasma flow and electric field inferred from Helioseismic Magnetic Imager vector magnetic field measurements. Astrophys. J. **871**, L28.
44. Jiang, C., Wu, S.T., Feng, X., and Hu, Q. (2016). Data-driven magnetohydrodynamic modelling of a flux-emerging active region leading to solar eruption. Nat. Commun. **7**, 11522.
45. Li, H., Feng, X., Zuo, P., and Wei, F. (2020). Simulation of the interplanetary B_z using a data-driven heliospheric solar wind model. Astrophys. J. **900**, 76.
46. Liu, C., Chen, T., and Zhao, X. (2019). New data-driven method of simulating coronal mass ejections. Astron. Astrophys. **626**, A91.
47. Warnecke, J., and Peter, H. (2019). Data-driven model of the solar corona above an active region. Astron. Astrophys. **624**, L12.
48. Wu, S.T., Wang, A.H., Liu, Y., and Hoeksema, J.T. (2006). Data-driven magnetohydrodynamic model for active region evolution. Astrophys. J. **652**, 800–811.
49. Wu, S.T., Wang, A.H., and Falconer, D.A. (2004). A three-dimensional magnetohydrodynamic (MHD) model of active region evolution. Proc. IAU **2004**, 291–301.

50. Yang, L.P., Feng, X.S., Xiang, C.Q., et al. (2012). Time-dependent MHD modeling of the global solar corona for year 2007: driven by daily-updated magnetic field synoptic data: time-dependent MHD modeling of corona. J. Geophys. Res. **117**, A08110.

51. Yang, W.H., Sturrock, P.A., and Antiochos, S.K. (1986). Force-free magnetic fields - the magneto-frictional method. Astrophys. J. **309**, 383.

52. Yee, K. (1966). Numerical solution of initial boundary value problems involving Maxwell's equations in isotropic media. IEEE Trans. Antennas Propagat. **14**, 302−307.

53. Yeates, A.R. (2022). On the limitations of magneto-frictional relaxation. Geophys. Astrophys. Fluid Dyn. 1−16. https://doi.org/10.1080/03091929.2021.2021197.

54. Jiang, C., and Feng, X. (2013). Extrapolation of the solar coronal magnetic field from SDO/HMI magnetogram by a CESE-MHD-NLFFF code. Astrophys. J. **769**, 144.

55. Török, T., and Kliem, B. (2005). Confined and ejective eruptions of kink-unstable flux ropes. Astrophys. J. **630**, L97−L100.

56. Török, T., and Kliem, B. (2003). The evolution of twisting coronal magnetic flux tubes. Astron. Astrophys. **406**, 1043−1059.

57. Keppens, R., Meliani, Z., van Marle, A.J., et al. (2012). Parallel, grid-adaptive approaches for relativistic hydro and magnetohydrodynamics. J. Comput. Phys. **231**, 718−744.

58. Xia, C., Teunissen, J., Mellah, I.E., et al. (2018). MPI-AMRVAC 2.0 for solar and astrophysical applications. Astrophys. J. Suppl. Ser. **234**, 30.

59. Peter, H., Warnecke, J., Chitta, L.P., and Cameron, R.H. (2015). Limitations of force-free magnetic field extrapolations: revisiting basic assumptions. Astron. Astrophys. **584**, A68.

60. Hayashi, K., Feng, X., Xiong, M., and Jiang, C. (2018). An MHD simulation of solar active region 11158 driven with a time-dependent electric field determined from HMI vector magnetic field measurement data. Astrophys. J. **855**, 11.

61. Jiang, C., Bian, X., Sun, T., and Feng, X. (2021). MHD modeling of solar coronal magnetic evolution driven by photospheric flow. Front. Phys. **9**, 646750.

62. Feng, X., Ma, X., and Xiang, C. (2015). Data-driven modeling of the solar wind from 1 R_s to 1 AU: data-driven solar wind modeling. J. Geophys. Res. Space Phys. **120**, 10159−10174.

63. Hoeksema, J.T., Abbett, W.P., Bercik, D.J., et al. (2020). The coronal global evolutionary model: using HMI vector magnetogram and Doppler data to determine coronal magnetic field evolution. Astrophys. J. Suppl. Ser. **250**, 28.

64. Abbett, W.P. (2007). The magnetic connection between the convection zone and corona in the quiet sun. Astrophys. J. **665**, 1469−1488.

65. Xia, C. (2018). Radiative magnetohydrodynamics simulations on solar corona. Sci. Sin.-Phys. Mech. Astron. **48**, 089501.

66. Jiang, C., Wu, S.T., and Feng, X. (2016). Analyses of the photospheric magnetic dynamics in solar active region 11117 using an advanced CESE-MHD model. Front. Astron. Space Sci. **3**, 16.

67. Harten, A. (1983). High resolution schemes for hyperbolic conservation laws. J. Comput. Phys. **49**, 357−393.

68. van Leer, B. (1979). Towards the ultimate conservative difference scheme. V. a second-order sequel to Godunov's method. J. Comput. Phys. **32**, 101−136.

69. Feng, X., Hu, Y., and Wei, F. (2006). Modeling the resistive MHD by the CESE method. Solar Phys. **235**, 235−257.

70. Jiang, C., Feng, X., Zhang, J., and Zhong, D. (2010). AMR simulations of magnetohydrodynamic problems by the CESE method in curvilinear coordinates. Solar Phys. **267**, 463−491.

71. Zhang, Z.-C., Yu, S.T.J., and Chang, S.-C. (2002). A space-time conservation element and solution element method for solving the two- and three-dimensional unsteady Euler equations using quadrilateral and hexahedral meshes. J. Comput. Phys. **175**, 168−199.

72. Leake, J.E., Linton, M.G., and Schuck, P.W. (2017). Testing the accuracy of data driven MHD simulations of active region evolution. Astrophys. J. **838**, 113.

73. Amari, T., Canou, A., and Aly, J.-J. (2014). Characterizing and predicting the magnetic environment leading to solar eruptions. Nature **514**, 465−469.

74. Jiang, C., Wu, S.T., Feng, X., and Hu, Q. (2013). Formation and eruption of an active region sigmoid. I. a study by nonlinear force-free field modeling. Astrophys. J. **780**, 55.

75. Sun, X., Hoeksema, J.T., Liu, Y., et al. (2012). Evolution of magnetic field and energy in a major eruptive active region based on SDO/HMI observation. Astrophys. J. **748**, 77.

76. Fan, Y.-L., Wang, H.-N., He, H., and Zhu, X.-S. (2012). Application of a data-driven simulation method to the reconstruction of the coronal magnetic field. Res. Astron. Astrophys. **12**, 563−572.

77. Jiang, C., Feng, X., Wu, S.T., and Hu, Q. (2012). Study of the three-dimensional coronal magnetic field of active region 11117 around the time of a confined flare using a data-driven CESE-MHD model. Astrophys. J. **759**, 85.

78. Wu, S.T., Wang, A.H., Gary, G.A., et al. (2009). Analyses of magnetic field structures for active region 10720 using a data-driven 3D MHD model. Adv. Space Res. **44**, 46−53.

79. Samanta, T., Tian, H., Chen, B., et al. (2021). Plasma heating induced by tadpole-like downflows in the flaring solar corona. Innovation **2**, 100083.

80. Chitta, L.P., Kariyappa, R., van Ballegooijen, A.A., et al. (2014). Nonlinear force-free field modeling of the solar magnetic carpet and comparison with SDO/HMI and SUNRISE/IMAX observations. Astrophys. J. **793**, 112.

81. Meyer, K.A., Mackay, D.H., Talpeanu, D.-C., et al. (2020). Investigation of the middle corona with SWAP and a data-driven non-potential coronal magnetic field model. Solar Phys. **295**, 101.

82. Seaton, D.B., De Groof, A., Shearer, P., et al. (2013). SWAP observations of the long-term, large-scale evolution of the extreme-ultraviolet solar corona. Astrophys. J. **777**, 72.

83. Cheng, X., Guo, Y., and Ding, M. (2017). Origin and structures of solar eruptions I: magnetic flux rope. Sci. China Earth Sci. **60**, 1383−1407.

84. Duan, A., Jiang, C., He, W., et al. (2019). A study of pre-flare solar coronal magnetic fields: magnetic flux ropes. Astrophys. J. **884**, 73.

85. Duan, A., Jiang, C., Zhou, et al. (2021). Variation of magnetic flux ropes through major solar flares. Astrophys. J. **907**, L23.

86. Kliem, B., Lee, J., Liu, R., et al. (2021). Nonequilibrium flux rope formation by confined flares preceding a solar coronal mass ejection. Astrophys. J. **909**, 91.

87. Liu, R. (2020). Magnetic flux ropes in the solar corona: structure and evolution toward eruption. Res. Astron. Astrophys. **20**, 165.

88. Patsourakos, S., Vourlidas, A., Török, T., et al. (2020). Decoding the pre-eruptive magnetic field configurations of coronal mass ejections. Space Sci. Rev. **216**, 131.

89. Xing, C., Cheng, X., and Ding, M. (2020). Evolution of the toroidal flux of CME flux ropes during eruption. Innovation **1**, 100059.

90. van Ballegooijen, A.A., and Martens, P.C.H. (1989). Formation and eruption of solar prominences. Astrophys. J. **343**, 971.

91. Pariat, E., Leake, J.E., Valori, G., et al. (2017). Relative magnetic helicity as a diagnostic of solar eruptivity. Astron. Astrophys. **601**, A125.

92. Zuccarello, F.P., Pariat, E., Valori, G., and Linan, L. (2018). Threshold of non-potential magnetic helicity ratios at the onset of solar eruptions. Astrophys. J. **863**, 41.

93. Kliem, B., and Török, T. (2006). Torus instability. Phys. Rev. Lett. **96**, 255002.

94. Fisher, G.H., Abbett, W.P., Bercik, D.J., et al. (2015). The coronal global evolutionary model: using HMI vector magnetogram and Doppler data to model the buildup of free magnetic energy in the solar corona: CGEM. Space Weather **13**, 369−373.

95. Bhattacharjee, A., Huang, Y.-M., Yang, H., and Rogers, B. (2009). Fast reconnection in high-Lundquist-number plasmas due to the plasmoid Instability. Phys. Plasmas **16**, 112102.

96. Antiochos, S.K., DeVore, C.R., and Klimchuk, J.A. (1999). A model for solar coronal mass ejections. Astrophys. J. **510**, 485−493.

97. Jiang, C., Feng, X., Liu, R., et al. (2021). A fundamental mechanism of solar eruption initiation. Nat. Astron. **5**, 1126−1138.

98. Lin, J., and Forbes, T.G. (2000). Effects of reconnection on the coronal mass ejection process. J. Geophys. Res. **105**, 2375−2392.

99. Wyper, P.F., Antiochos, S.K., and DeVore, C.R. (2017). A universal model for solar eruptions. Nature **544**, 452−455.

100. Pagano, P., Mackay, D.H., and Poedts, S. (2013). Magnetohydrodynamic simulations of the ejection of a magnetic flux rope. Astron. Astrophys. **554**, A77.

101. Jiang, C., Feng, X., Wu, S.T., and Hu, Q. (2013). Magnetohydrodynamic simulation of a sigmoid eruption of active region 11283. Astrophys. J. **771**, L30.

102. Jiang, C., Feng, X., and Xiang, C. (2012). A new code for nonlinear force-free field extrapolation of the global corona. Astrophys. J. **755**, 62.

103. Jiang, C., and Feng, X. (2012). A new implementation of the magnetohydrodynamics-relaxation method for nonlinear force-free field extrapolation in the solar corona. Astrophys. J. **749**, 135.

104. Lemen, J.R., Title, A.M., Akin, D.J., et al. (2012). The atmospheric imaging assembly (AIA) on the solar dynamics observatory (SDO). Solar Phys. **275**, 17−40.

105. Inoue, S. (2016). Magnetohydrodynamics modeling of coronal magnetic field and solar eruptions based on the photospheric magnetic field. Prog. Earth Planet. Sci. **3**, 19.

106. Inoue, S., Hayashi, K., Magara, T., et al. (2014). Magnetohydrodynamic simulation of the X2.2 SOLAR flare on 2011 February 15. I. comparison with the observations. Astrophys. J. **788**, 182.

107. Inoue, S., Hayashi, K., Magara, T., et al. (2015). Magnetohydrodynamic simulation of the X2.2 solar flare on 2011 February 15. II. dynamics connecting the solar flare and the coronal mass ejection. Astrophys. J. **803**, 73.

108. Inoue, S., and Bamba, Y. (2021). An MHD modeling of the successive X2.2 and X9.3 solar flares of 2017 September 6. Astrophys. J. **914**, 71.

109. Jiang, C., Zou, P., Feng, X., et al. (2018). Magnetohydrodynamic simulation of the X9.3 flare on 2017 September 6: evolving magnetic topology. Astrophys. J. **869**, 13.

110. Kliem, B., Su, Y.N., van Ballegooijen, A.A., and DeLuca, E.E. (2013). Magnetohydrodynamic modeling of the solar eruption on 2010 April 8. Astrophys. J. **779**, 129.

111. Prasad, A., Bhattacharyya, R., and Kumar, S. (2017). Magnetohydrodynamic modeling of solar coronal dynamics with an initial non-force-free magnetic field. Astrophys. J. **840**, 37.

112. Xue, Z., Yan, X., Cheng, X., et al. (2016). Observing the release of twist by magnetic reconnection in a solar filament eruption. Nat. Commun. **7**, 11837.

113. van Ballegooijen, A.A. (2004). Observations and modeling of a filament on the sun. Astrophys. J. **612**, 519−529.

114. van Ballegooijen, A.A., DeLuca, E.E., Squires, K., and Mackay, D.H. (2007). Modeling magnetic flux ropes in the solar atmosphere. J. Atmos. Solar-Terrestrial Phys. **69**, 24−31.

115. Su, Y., van Ballegooijen, A., Lites, B.W., et al. (2009). Observations and nonlinear force-free field modeling of active region 10953. Astrophys. J. **691**, 105−114.

116. Su, Y., van Ballegooijen, A., Schmieder, B., et al. (2009). Flare energy build-up in a decaying active region near a coronal hole. Astrophys. J. **704**, 341−353.

117. Su, Y., Surges, V., van Ballegooijen, A., et al. (2011). Observations and magnetic field modeling of the flare/coronal mass ejection event on 2010 April 8. Astrophys. J. **734**, 53.

118. Su, Y., and van Ballegooijen, A. (2012). Observations and magnetic field modeling of a solar polar crown prominence. Astrophys. J. **757**, 168.

119. Nayak, S.S., Bhattacharyya, R., Prasad, A., et al. (2019). A data-constrained magnetohydrodynamic simulation of successive events of blowout jet and C-class flare in NOAA AR 12615. Astrophys. J. **875**, 10.

120. Prasad, A., Bhattacharyya, R., Hu, Q., et al. (2018). A magnetohydrodynamic simulation of magnetic null-point reconnections in NOAA AR 12192, initiated with an extrapolated non-force-free field. Astrophys. J. **860**, 96.

121. Prasad, A., Dissauer, K., Hu, Q., et al. (2020). Magnetohydrodynamic simulation of magnetic null-point reconnections and coronal dimmings during the X2.1 flare in NOAA AR 11283. Astrophys. J. **903**, 129.

122. Hu, Q., Dasgupta, B., Choudhary, D.P., and Büchner, J. (2008). A practical approach to coronal magnetic field extrapolation based on the principle of minimum dissipation rate. Astrophys. J. **679**, 848–853.

123. Hu, Q., Dasgupta, B., DeRosa, M.L., et al. (2010). Non-force-free extrapolation of solar coronal magnetic field using vector magnetograms. J. Atmos. Solar-Terrestrial Phys. **72**, 219–223.

124. Hu, Q., and Dasgupta, B. (2008). An improved approach to non-force-free coronal magnetic field extrapolation. Solar Phys. **247**, 87–101.

125. Moore, R.L., Sterling, A.C., Hudson, H.S., and Lemen, J.R. (2001). Onset of the magnetic explosion in solar flares and coronal mass ejections. Astrophys. J. **552**, 833–848.

126. Aulanier, G., Török, T., Démoulin, P., and DeLuca, E.E. (2010). Formation of torus-unstable flux ropes and electric currents in erupting sigmoids. Astrophys. J. **708**, 314–333.

127. Démoulin, P., and Aulanier, G. (2010). Criteria for flux rope eruption: non-equilibrium versus torus instability. Astrophys. J. **718**, 1388–1399.

128. Fan, Y. (2010). On the eruption of coronal flux ropes. Astrophys. J. **719**, 728–736.

129. Zuccarello, F.P., Aulanier, G., and Gilchrist, S.A. (2015). Critical decay index at the onset of solar eruptions. Astrophys. J. **814**, 126.

130. Suematsu, Y., Tsuneta, S., Ichimoto, K., et al. (2009). The solar optical telescope of solar-B (Hinode): the optical telescope assembly. In The Hinode Mission, T. Sakurai, ed. (Springer), pp. 143–166.

131. Tsuneta, S., Ichimoto, K., Katsukawa, Y., et al. (2008). The solar optical telescope for the Hinode mission: an overview. Solar Phys. **249**, 167–196.

132. Amari, T., Boulmezaoud, T.Z., and Mikic, Z. (1999). An iterative method for the reconstruction of the solar coronal magnetic field. Astron. Astrophys. **350**, 1051–1059.

133. Amari, T., Boulmezaoud, T.Z., and Aly, J.J. (2006). Well posed reconstruction of the solar coronal magnetic field. Astron. Astrophys. **446**, 691–705.

134. Amari, T., Canou, A., Delyon, F., et al. (2011). Reconstruction of the solar coronal magnetic field, from active region to large scale. In SF2A-2011: Proceedings of the Annual Meeting of the French Society of Astronomy and Astrophysics, G. Alecian, K. Belkacem, R. Samadi, and D. Valls-Gabaud, eds., pp. 389–394. https://ui.adsabs.harvard.edu/abs/2011sf2a.conf..389A.

135. Amari, T., Canou, A., Aly, J.-J., et al. (2018). Magnetic cage and rope as the key for solar eruptions. Nature **554**, 211–215.

136. Chen, H., Zhang, J., Ma, S., et al. (2015). Confined flares in solar active region 12192 from 2014 October 18 to 29. Astrophys. J. **808**, L24.

137. Sun, X., Bobra, M.G., Hoeksema, J.T., et al. (2015). Why is the great solar active region 12192 flare-rich but CME-poor? Astrophys. J. **804**, L28.

138. Muhamad, J., Kusano, K., Inoue, S., and Shiota, D. (2017). Magnetohydrodynamic simulations for studying solar flare trigger mechanism. Astrophys. J. **842**, 86.

139. Kusano, K., Maeshiro, T., Yokoyama, T., and Sakurai, T. (2004). The trigger mechanism of solar flares in a coronal arcade with reversed magnetic shear. Astrophys. J. **610**, 537–549.

140. Jiang, C., Feng, X., and Hu, Q. (2018). Formation and eruption of an active region sigmoid. II. magnetohydrodynamic simulation of a multistage eruption. Astrophys. J. **866**, 96.

141. Dai, Y., Ding, M.D., and Guo, Y. (2013). Production of the extreme-ultraviolet late phase of an X class flare in a three-stage magnetic reconnection process. Astrophys. J. **773**, L21.

142. Zhong, Y., Dai, Y., and Ding, M.D. (2021). Extreme-ultraviolet late phase in homologous solar flares from a complex active region. Astrophys. J. **916**, 37.

143. Hou, Y.J., Zhang, J., Li, T., et al. (2018). Eruption of a multi-flux-rope system in solar active region 12673 leading to the two largest flares in Solar Cycle 24. Astron. Astrophys. **619**, A100.

144. Yan, X., Xue, Z., Jiang, C., et al. (2022). Fast plasmoid-mediated reconnection in a solar flare. Nat. Commun. **13**, 640.

145. Liu, Z., Xu, J., Gu, B.-Z., et al. (2014). New vacuum solar telescope and observations with high resolution. Res. Astron. Astrophys. **14**, 705–718.

146. Titov, V.S., Hornig, G., and Démoulin, P. (2002). Theory of magnetic connectivity in the solar corona. J. Geophys. Res. **107**, 1164.

147. DeRosa, M.L., Schrijver, C.J., Barnes, G., et al. (2009). A critical assessment of nonlinear force-free field modeling of the solar corona for active region 10953. Astrophys. J. **696**, 1780–1791.

148. DeRosa, M.L., Wheatland, M.S., Leka, K.D., et al. (2015). The influence of spatial resolution on nonlinear force-free modeling. Astrophys. J. **811**, 107.

149. Schrijver, C.J., Derosa, M.L., Metcalf, T.R., et al. (2006). Nonlinear force-free modeling of coronal magnetic fields part I: a quantitative comparison of methods. Solar Phys. **235**, 161–190.

150. Schrijver, C.J., DeRosa, M.L., Metcalf, T., et al. (2008). Nonlinear force-free field modeling of a solar active region around the time of a major flare and coronal mass ejection. Astrophys. J. **675**, 1637–1644.

151. He, W., Jiang, C., Zou, P., et al. (2020). Data-driven MHD simulation of the formation and initiation of a large-scale preflare magnetic flux rope in AR 12371. Astrophys. J. **892**, 9.

152. Jiang, C., Wu, S.T., Yurchyshyn, V., et al. (2016). How did a major confined flare occur in super solar active region 12192? Astrophys. J. **828**, 62.

153. Cao, W., Gorceix, N., Coulter, R., et al. (2010). Scientific instrumentation for the 1.6 m new solar telescope in big bear. Astron. Nachr. **331**, 636–639.

154. Yan, X.L., Jiang, C.W., Xue, Z.K., et al. (2017). The eruption of a small-scale emerging flux rope as the driver of an M-class flare and of a coronal mass ejection. Astrophys. J. **845**, 18.

155. Inoue, S., Hayashi, K., and Kusano, K. (2016). Structure and stability of magnetic fields in solar active region 12192 based on nonlinear force-free field modeling. Astrophys. J. **818**, 168.

156. Cheng, X., Zhang, J., Kliem, B., et al. (2020). Initiation and early kinematic evolution of solar eruptions. Astrophys. J. **894**, 85.

157. Jing, J., Liu, C., Lee, J., et al. (2018). Statistical analysis of torus and kink instabilities in solar eruptions. Astrophys. J. **864**, 138.

158. Zhao, J., Gilchrist, S.A., Aulanier, G., et al. (2016). Hooked flare ribbons and flux-rope related QSL footprints. Astrophys. J. **823**, 62.

159. Guo, Y., Schmieder, B., Démoulin, P., et al. (2010). Coexisting flux rope and dipped arcade sections along one solar filament. Astrophys. J. **714**, 343–354.

160. Canou, A., and Amari, T. (2010). A twisted flux rope as the magnetic structure of a filament in active region 10953 observed by Hinode. Astrophys. J. **715**, 1566–1574.

161. Metcalf, T.R., DeRosa, M.L., Schrijver, C.J., et al. (2008). Nonlinear force-free modeling of coronal magnetic fields. II. modeling a filament arcade and simulated chromospheric and photospheric vector fields. Solar Phys. **247**, 269–299.

162. Toriumi, S., Takasao, S., Cheung, M.C.M., et al. (2020). Comparative study of data-driven solar coronal field models using a flux emergence simulation as a ground-truth data set. Astrophys. J. **890**, 103.

163. Jiang, C., and Toriumi, S. (2020). Testing a data-driven active region evolution model with boundary data at different heights from a solar magnetic flux emergence simulation. Astrophys. J. **903**, 11.

164. Metcalf, T.R., Jiao, L., McClymont, A.N., et al. (1995). Is the solar chromospheric magnetic field force-free? Astrophys. J. **439**, 474.

165. Moon, Y.-J., Choe, G.S., Yun, H.S., et al. (2002). Force-freeness of solar magnetic fields in the photosphere. Astrophys. J. **568**, 422–431.

166. Tiwari, S.K. (2012). On the force-free nature of photospheric sunspot magnetic fields as observed from Hinode (SOT/SP). Astrophys. J. **744**, 65.

167. Wang, H., and Liu, C. (2015). Structure and evolution of magnetic fields associated with solar eruptions. Res. Astron. Astrophys. **15**, 145–174.

168. Toriumi, S., and Wang, H. (2019). Flare-productive active regions. Living Rev. Sol. Phys. **16**, 3.

169. Bi, Y., Jiang, Y., Yang, J., et al. (2016). Observation of a reversal of rotation in a sunspot during a solar flare. Nat. Commun. **7**, 13798.

170. Liu, C., Xu, Y., Cao, W., et al. (2016). Flare differentially rotates sunspot on Sun's surface. Nat. Commun. **7**, 13104.

171. Duan, A., Jiang, C., Toriumi, S., and Syntelis, P. (2020). On the lorentz force and torque of solar photospheric emerging magnetic fields. Astrophys. J. **896**, L9.

172. Hotta, H., and Iijima, H. (2020). On rising magnetic flux tube and formation of sunspots in a deep domain. Monthly Notices R. Astronomical Soc. **494**, 2523–2537.

173. Toriumi, S., and Hotta, H. (2019). Spontaneous generation of δ-sunspots in convective magnetohydrodynamic simulation of magnetic flux emergence. Astrophys. J. **886**, L21.

174. Cheung, M.C.M., and Isobe, H. (2014). Flux emergence (theory). Living Rev. Solar Phys. **11**, 3.

175. Charbonneau, P. (2020). Dynamo models of the solar cycle. Living Rev. Solar Phys. **17**, 4.

176. Cheung, M.C.M., Rempel, M., Chintzoglou, G., et al. (2019). A comprehensive three-dimensional radiative magnetohydrodynamic simulation of a solar flare. Nat. Astron. **3**, 160–166.

177. Jin, M., Manchester, W.B., van der Holst, B., et al. (2017). Data-constrained coronal mass ejections in a global magnetohydrodynamics model. Astrophys. J. **834**, 173.

178. Lugaz, N., Downs, C., Shibata, K., et al. (2011). Numerical investigation of a coronal mass ejection from an anemone active region: reconnection and deflection of the 2005 August 22 eruption. Astrophys. J. **738**, 127.

179. Lugaz, N., Manchester IV, W.B., and Gombosi, T.I. (2005). Numerical simulation of the interaction of two coronal mass ejections from Sun to Earth. Astrophys. J. **634**, 651–662.

180. Manchester, W.B., Gombosi, T.I., Roussev, I., et al. (2004). Modeling a space weather event from the Sun to the Earth: CME generation and interplanetary propagation: CME propagation to 1 AU. J. Geophys. Res. **109**, A02107.

181. Shen, F., Shen, C., Zhang, J., et al. (2014). Evolution of the 12 July 2012 CME from the Sun to the Earth: data-constrained three-dimensional MHD simulations: 3D simulation to 2012 July 12 CME event. J. Geophys. Res. Space Phys. **119**, 7128–7141.

182. DeRosa, M.L., and Barnes, G. (2018). Does nearby open flux affect the eruptivity of solar active regions? Astrophys. J. **861**, 131.

183. Wu, S.T., Zhou, Y., Jiang, C., et al. (2016). A data-constrained three-dimensional magnetohydrodynamic simulation model for a coronal mass ejection initiation. J. Geophys. Res. Space Phys. **121**, 1009–1023.

184. Hayashi, K., Abbett, W.P., Cheung, M.C.M., and Fisher, G.H. (2021). Coupling a global heliospheric magnetohydrodynamic model to a magnetofrictional model of the low corona. Astrophys. J. Suppl. Ser. **254**, 1.

185. Fox, N.J., Velli, M.C., Bale, S.D., et al. (2016). The solar probe plus mission: humanity's first visit to our star. Space Sci. Rev. **204**, 7–48.

186. Kasper, J.C., Klein, K.G., Lichko, E., et al. (2021). *Parker Solar Probe* enters the magnetically dominated solar corona. Phys. Rev. Lett. **127**, 255101.

187. Müller, D., Marsden, R.G., St. Cyr, O.C., and Gilbert, H.R. (2013). Solar Orbiter: exploring the sun–heliosphere connection. Solar Phys. **285**, 25–70.

188. Kusano, K., Bamba, Y., Yamamoto, T.T., et al. (2012). Magnetic field structures triggering solar flares and coronal mass ejections. Astrophys. J. **760**, 31.

189. Wang, H., Liu, C., Ahn, K., et al. (2017). High-resolution observations of flare precursors in the low solar atmosphere. Nat. Astron. **1**, 0085.

190. Rimmele, T.R., Warner, M., Keil, S.L., et al. (2020). The Daniel K. Inouye solar telescope – observatory overview. Sol. Phys. **295**, 172.

191. Valori, G., Löschl, P., Stansby, D., et al. (2022). Disambiguation of vector magnetograms by stereoscopic observations from the solar orbiter (SO)/Polarimetric and helioseismic

imager (PHI) and the solar dynamic observatory (SDO)/Helioseismic and magnetic imager (HMI). Sol. Phys. **297**, 12.

192. van der Holst, B., Manchester, W.B., Frazin, R.A., et al. (2010). A data-driven, two-temperature solar wind model with alfvén waves. Astrophys. J. **725**, 1373–1383.

193. Amari, T., Luciani, J.-F., Aly, J.-J., and Tagger, M. (1996). Plasmoid formation in a single sheared arcade and application to coronal mass ejections. Astron. Astrophys. **306**, 913.

194. Choe, G.S., and Lee, L.C. (1996). Evolution of solar magnetic arcades. II. effect of resistivity and solar eruptive processes. Astrophys. J. **472**, 372–388.

195. Mikic, Z., and Linker, J.A. (1994). Disruption of coronal magnetic field arcades. Astrophys. J. **430**, 898.

196. Aly, J.J. (1991). How much energy can be stored in a three-dimensional force-free magnetic field? Astrophys. J. **375**, L61.

197. Sturrock, P.A. (1991). Maximum energy of semi-infinite magnetic field configurations. Astrophys. J. **380**, 655.

AUTHOR CONTRIBUTIONS

C.J. wrote the manuscript. All authors read and revised the manuscript.

DECLARATION OF INTERESTS

The authors declare no competing interests.

SUPPLEMENTAL INFORMATION

Supplemental information can be found online at https://doi.org/10.1016/j.xinn.2022.100236.